

8–13 μm spectroscopy of luminous and ultraluminous infrared galaxies

C. C. Dudley

Institute for Astronomy, University of Hawaii, 2680 Woodlawn Dr., Honolulu, Hawaii 96822, USA

ABSTRACT

New moderate-resolution mid-infrared spectroscopy at 10 μm of 27 infrared galaxies is presented. The galaxies have been chosen from three 60 μm selected and one 12 μm selected complete flux-limited catalogs of galaxies; 17 of these sources have $L_{\text{IR}}(8\text{--}1000\mu\text{m}) \geq 5 \times 10^{11} L_{\odot}$. A high-resolution spectrum of the source Arp 299B1 is also presented. Combining these new results with previously published results, a nearly complete 60 μm selected flux limited subsample, with $L_{\text{IR}}(8\text{--}1000\mu\text{m}) \geq 1.6 \times 10^{11} L_{\odot}$ of 25 galaxies is defined. Within this subsample, it is found that the dominant power source of infrared galaxies in the luminosity range $1.6 \times 10^{11} < L_{\text{IR}}(8\text{--}1000\mu\text{m}) < 10^{12} L_{\odot}$ is massive star formation based on the clear presence of the 11.3 μm aromatic hydrocarbon emission feature in the majority of the spectra. Three of the five ultraluminous infrared galaxies ($L_{\text{IR}}(8\text{--}1000\mu\text{m}) \geq 10^{12} L_{\odot}$) within this subsample show evidence that an active galactic nucleus provides an energetically important power source based on the detection of silicate absorption in their mid-infrared spectra. The physical basis of a possible anti-correlation between the 11.3 μm feature equivalent width and infrared light to molecular gas mass ratios is discussed.

Key words: dust – infrared: galaxies – galaxies: starburst, active

1 INTRODUCTION

This work is aimed at the question of what provides the dominant power source of ultraluminous infrared galaxies, that is galaxies with luminosities in the wavelength range 8–1000 μm in excess of $10^{12} L_{\odot}$ ($H_0=75 \text{ km s}^{-1} \text{ Mpc}^{-1}$). This question is of interest because it is possible that the power source of these galaxies is qualitatively different from the dominant power source of most infrared galaxies of lower luminosity. The observational approach of this work is the use of moderate resolution 8–13 μm spectroscopy.

In very broad strokes, the context of the debate over the question addressed here can be summarized as an attempt, on the one hand, to explain ultraluminous infrared galaxies as more powerful versions of starburst galaxies, that is as super starbursts (Joseph & Wright 1985), where massive star formation provides the power source, and on the other hand, to demonstrate that ultraluminous infrared galaxies are the precursors of quasars (Sanders et al. 1988) and are powered by active galactic nuclei (AGNs).

The question has remained open to serious debate for essentially one reason: dust. Infrared galaxies by their nature radiate the bulk of their energy through the degradation of the optical and UV photons emitted by the primary power source into infrared photons emitted by dust heated to a temperature of ~ 50 K. This has the effect of erasing most

of the commonly accepted features used to distinguish the characteristics of starbursts and AGNs.

Optical and, to a lesser degree, near-infrared studies are particularly susceptible to this difficulty since spectroscopic signatures of AGNs in ultraluminous infrared galaxies should only betray sources that are relatively unobscured and therefore might not contribute substantially to the heating of the dust that is the final source of most of the observed emission. However, Veilleux et al. (1995) have shown in a large sample of infrared galaxies that the fraction of infrared galaxies with AGN-like optical spectra increases as a function of increasing luminosity, providing important circumstantial evidence that AGN-like activity is associated with ultraluminous infrared galaxies. The strength of this evidence might be considered to be weakened, however, by the finding of Goldader et al. (1995) that the ratio of Br γ to infrared luminosity decreases as a function of luminosity, suggesting that dust obscuration plays an even greater role in ultraluminous infrared galaxies than in luminous infrared galaxies. This suggests the perverse possibility that energetically dominant starbursts in ultraluminous infrared galaxies are so obscured in the optical that only incidental unobscured AGNs are detected.

Radio observations are unaffected by dust obscuration and can provide high spatial resolution. However, the pri-

marily synchrotron radiation that is detected is only indirectly linked to the power source of infrared galaxies. In starbursts, it is thought that the radio emission arises from electrons accelerated in supernovae remnants, while in AGN, relativistic jets are strong radio emitters. Condon et al. (1991; hereafter CHYT) have employed the high spatial resolution provided by the Very Large Array (VLA) to show that the radio sizes of a large fraction of ultraluminous infrared galaxies are comparable to the minimum size required for a blackbody that reproduces the 25, 60, and 100 μm flux densities of these sources. From this they infer that starbursts rather than AGNs may power these sources. At even higher spatial resolution provided by very long baseline interferometry (VLBI), Lonsdale, Smith & Lonsdale (1993) find evidence for radio structure on the scale of milliarcseconds, some components of which have brightness temperatures well in excess of what could be expected in starburst-related emission. They deduce from this that AGNs are present in five of eight of the ultraluminous infrared galaxies in their sample*.

In this work, the dust emission itself is examined for spectral clues that can reveal the nature of the power source in infrared galaxies. In a sample of 60 galaxies, Roche et al. (1991; hereafter RASW) have shown that their 8–13 μm spectra can be classified into three types: those with prominent polycyclic aromatic hydrocarbon (PAH) features generally show H II region-like optical spectra, those with flat featureless spectra have Seyfert 1 or quasar-like optical spectra, and those rare galaxies with silicate absorption features usually have Seyfert 2 optical spectra. Dudley & Wynn-Williams (1997) have extended the work on galaxies with very deep silicate features to show that the size of the power source can be constrained to be smaller than a few parsecs, implying that such sources are powered by deeply embedded AGNs. Here, the 8–13 μm spectra of a well-defined sample of 25 luminous and ultraluminous infrared galaxies are examined in this context.

It should be noted that all of the sources for which new spectral observations are reported here can be found in one or more of four *IRAS*-based catalogs: the Bright Galaxy Survey (Soifer et al. 1989), the Extended Bright Galaxy Survey (Sanders et al. 1995), the Two Jansky Survey (Strauss et al. 1992), or the Extended 12 μm Survey (Rush, Malkan & Spinoglio 1993).

Observations and data reduction procedures are described in Section 2. Section 3 presents the new spectral observations. The classification of the spectra is discussed in Section 4.1. The justification for the classification of the ultraluminous galaxies that fall within the later subsample is discussed in some detail in Section 4.2. In Section 4.3 a subsample of galaxies is defined and an apparent trend with luminosity within it is examined. The possibility of an anti-correlation between the equivalent width of the 11.3 μm PAH feature and the ratio of infrared light to molecular gas mass is discussed in Section 4.4, and conclusions are drawn in Section 5.

* Smith, Lonsdale & Lonsdale (1998) suggest that radio supernova remnants may be responsible for some of the structure they detect

2 OBSERVATIONS AND DATA REDUCTION

The new observations reported here were obtained over the course of 5 years, from 1991 through 1995, using the 10 and 20 μm Cooled Grating Spectrograph (CGS3) mounted at the Cassegrain focus of the United Kingdom Infrared Telescope (UKIRT) on Mauna Kea in Hawaii. Observations in 1991 were obtained by G. Wynn-Williams and J. Goldader, in 1992 by G. Wynn-Williams and C. Dudley, and in 1993–1995 by C. Dudley. For parts of each observing run a UKIRT scientist (J. Davies, T. Geballe, or G. Wright) was present at the summit and participated in the observations. CGS3 has been described by Cohen & Davies (1995). All but one of the spectra reported here were obtained using the low-resolution spectroscopy mode with $\lambda/\Delta\lambda \sim 60$ in a series of beam-switched, chopped observations with a chop frequency of ~ 10 Hz and a beam switch frequency of ~ 0.5 Hz. To fully sample each spectrum, two interlacing grating positions were observed with changes between the two positions occurring after 10–16 beam-switched pairs. Table 1 gives a log of observations for the galaxies. In Table 1, column 1 is the object name, columns 2 and 3 give the aperture centre in RA and DEC, column 4 gives the position reference, columns 5 and 6 give the object redshift and reference, column 7 gives the date of observation, column 8 gives the circular aperture size used in arcseconds (full width at 10 per cent power), column 9 gives the chop throw in arcseconds, and column 10 gives the chop direction.

Observations were calibrated in wavelength by means of high order spectral measurements of a Kr lamp in the manner discussed by Hanner, Brooke & Tokunaga (1995). A master calibration spectrum was first selected and calibrated in wavelength by flattening a $2\times$ over-sampled Kr lamp spectrum (4 grating positions) with the spectrum of a soldering iron replacing the Kr lamp in the beam. Kr lamp spectra from each night's observations were then cross correlated against the unflattened master spectrum to give a wavelength calibration for each night. Typical shifts from the nominal CGS3 wavelength calibration were less than a resolution element, and were never more than 2 resolution elements.

Corrections for instrumental response, atmospheric transmission, and flux calibration were performed by dividing source spectra by the spectrum of a standard star with a known 10 μm flux density and an assumed blackbody temperature based on its spectral type, and then multiplying by the Planck curve of that temperature scaled to match the standard star in flux density. Observations of standard stars were performed with the same aperture, chop throw, position angle and frequency as the galaxy observations they calibrate. The standard star observations were made to match in airmass so that no additional airmass corrections would be required. For the standard stars, the number of beam-switched pairs between grating shifts was typically 3–5. The stars have been chosen, where possible, to have a spectral type of K0 or earlier to avoid the effects of SiO absorption, H⁻ opacity, and circumstellar dust emission that can effect the spectral shape of late-type stars. Table 2 gives the HR number, 10.1 μm flux density, photometric reference, and assumed blackbody temperature of each standard star, in columns 4, 5, 6, and 7, respectively, for each of the observations given in Table 1. In column 2 of Table 2, alternative

names are given for galaxies that are found in multiple catalogs, while column 3 gives the date of each observation as in Table 1. It should be noted that an error of ~ 1000 K in the assumed blackbody temperature of the standard stars leads to a ~ 2 per cent error in flux calibration at either end of the passband $8\text{--}13\ \mu\text{m}$ which is negligible for the purposes of this work, while for those stars of late spectral type, deviations from the assumed blackbody can be ~ 10 per cent in the SiO band (Cohen et al. 1995). Systematic uncertainties in overall flux calibration of $15\text{--}20$ per cent can arise due to telescope pointing errors with the stronger effects for the smaller apertures. For wavelengths shortward of $8.2\ \mu\text{m}$, strong systematic effects can occur as a result of a variable water vapor column in the Earth's atmosphere.

All spectra were regridded to a common wavelength scale using a Gaussian filter of $\sigma = 0.064\ \mu\text{m}$, which lead to a slight correlation between neighboring data points. Those spectra of the same source obtained on two or more nights were combined, weighted by integration time. Data not falling in the ranges $7.7\text{--}9.1$ and $10.0\text{--}13.4\ \mu\text{m}$ have been excluded due to poor atmospheric transmission.

Spectra of Wynn-Williams et al.'s (1991) Arp 299B1 were obtained on 1994 February 6 and 7 using CGS3 in high-resolution mode ($\lambda/\Delta\lambda \sim 250$) using a $3''.26$ full width at 10 per cent power circular aperture. The spectra obtained on each night were the result of two sets of observations each consisting of two interlacing grating positions but with different wavelength ranges to cover the spectral range $10\text{--}13.2\ \mu\text{m}$. The chop throw was $20''$, and the chop and beam switch PA were 45° . About 30 per cent of the first night's observations were affected by clouds; these data were rejected by inspecting the change in the dispersion of the total signal. The Kr lamp was observed on each night to provide wavelength calibration. The strongest lines from each night agreed in wavelength to 3 per cent of a resolution element so that the Kr spectra of the two nights were combined, and a difference in wavelength of 30 per cent of a resolution element was measured between the expected (based on the nominal calibration of CGS3) and the measured wavelengths of 5 Kr lines. An additive correction of $0.02\ \mu\text{m}$ was applied to the observations, this being the interpolation of the 2.117 and $2.191\ \mu\text{m}$ Kr lines measured at 6th order at the expected position of the galaxy [Ne II] line. Flux calibration was performed using HR 4067 with a $10.1\ \mu\text{m}$ flux density of 103 Jy and an assumed temperature of 4000 K on the first night, and HR 5340 using a $10.1\ \mu\text{m}$ flux density of 738 Jy and an assumed temperature of 4400 K on the second night. No significant difference was found between the two nights' observations, so they were combined according to their statistical weights. The difference in airmass between the source and standard observations was ~ 0.5 but monitoring of BS 4518 on the first night at airmasses similar to the source observations showed that the level of spectroscopic variation over the observed wavelength range as a function of airmass was negligible compared to the final signal-to-noise ratio. The overall photometric calibration is estimated to be good to about 25 per cent while the typical signal-to-noise ratio of an independent data point is about 10.

3 RESULTS

The intensity and equivalent width of the $11.3\ \mu\text{m}$ PAH feature have been measured directly for all of the sources by estimating the continuum in the rest wavelength (see Table 1) ranges $10.5\text{--}10.9$ and $11.7\text{--}12.1\ \mu\text{m}$ and subtracting the linear interpolation of these two estimates from the spectra to measure the residual flux in the range $10.9\text{--}11.7\ \mu\text{m}$. Uncertainties in the feature intensities represent the combined uncertainties in the residual flux in this range but not the uncertainties in continuum subtraction. For the equivalent width estimates, uncertainties in the continuum level have been included. In most cases the continuum uncertainties are dominant in the equivalent width estimates, leading to indeterminate results in the case of limits, but in a few cases the uncertainty in the residual is the dominant component, and upper limits to these equivalent widths can be set.

Since model fitting can lead to substantially cleaner estimates of feature fluxes (of order the signal-to-noise ratio in the peak spectral element being fit) estimates based on the model that is applied to these data to test for the presence of a silicate absorption feature are also given. The model consists of a power-law continuum and an additive PAH spectrum represented by the spectrum of the Orion Bar taken from Roche (1989). The fitting of this model was accomplished using a version of Bevington's (1969) program CURVEFIT supplied with IDL ver. 4.0 using three free parameters, the power-law continuum scaling and index ($f_\nu = \beta \times \nu^{-\alpha}$), and the scaling of the Orion Bar spectrum. The data were fit in the rest wavelength ranges $10.0\text{--}10.9$, $11.0\text{--}11.4$, and $11.7\text{--}12.6\ \mu\text{m}$ using initial guesses based on linear fits to the logarithm of data binned in the ranges $10.0\text{--}10.5$, $10.5\text{--}10.9$, and $11.7\text{--}12.6\ \mu\text{m}$ for the power-law scaling and index, and based on the continuum subtracted estimates of the flux in the $11.3\ \mu\text{m}$ feature. The weighting of the data was statistical. As discussed recently by Goldader et al. (1995), the use of a power-law as a fitting function tends to throw the bulk of the errors in the fit parameters into the power-law scaling, so that the formal errors of the remaining parameters are underestimated. Further, the model assumptions introduce further systematic uncertainties. In particular, by fitting the data in the range $11.2\text{--}12.6\ \mu\text{m}$, it is assumed that the ratio of $11.3\ \mu\text{m}$ feature emission with respect to the underlying plateau emission that extends to $12.9\ \mu\text{m}$ is the same as that found at the position of peak of the $11.3\ \mu\text{m}$ emission feature in the Orion Bar. This ratio, however, is known to vary spatially within the Orion Bar (Roche et al. 1989), and also within at least one external galaxy (Dudley & Wynn-Williams 1999). The consequences of this uncertainty are largest in spectra where the PAH emission is most powerful relative to the continuum. Given that the galaxy redshifts make it impossible to estimate the continuum beyond $13.1\ \mu\text{m}$ (rest frame) in ~ 50 per cent of the sources, it has not been possible to quantify the importance of this effect in these data, regardless of obvious signal-to-noise issues. Due to these multiple and tangled uncertainties, both results of direct measurements and model fits with formal errors are presented, but it must be cautioned that the model parameter errors are seriously underestimated. In particular, model $3\ \sigma$ upper limits to the $11.3\ \mu\text{m}$ intensity are roughly the same as measured $1\ \sigma$ upper

limits to the 11.3 μm intensity. The new spectra and model fits are presented in Fig. 1.

Table 3 presents the model power-law index in column 2, the measured (upper) and model (lower) 11.3 μm feature intensity in column 3, the 11.3 μm feature equivalent width in column 4, the ratio of the flux density of the source in the rest wavelength range 8.0–8.4 μm to the model flux density in the same range where the errors represent the errors in the estimates of the source flux densities only. Measurements of fine structure lines are given in columns 6 and 7. For the measurements of fine structure lines the continuum was estimated by eye, and for detections of the 12.8 μm [Ne II] line it must be cautioned that a significant amount of the intensity could be due to a blended PAH emission feature at 12.7 μm except in the case of Arp 299B1, where the spectral resolution is sufficient to distinguish the two features. Errors for detections and limits are 1 σ and 3 σ , respectively, except in the case of the model 11.3 μm equivalent width, which is reported in all cases to give a sense of the model continuum uncertainties. In the case of Arp 299B1, the fine structure [S IV] and [Ne II] results are derived from the high-resolution spectrum. The redshift of the [Ne II] line (2900 km s^{-1}) agrees within 1.4 σ (1 $\sigma = 170 \text{ km s}^{-1}$ based on Gaussian fitting) with the CO redshift measured by Sargent & Scoville (1991), while much more precise agreement between unpublished IRTF CSHELL Br γ data and the CO observations is known, so that some confidence in [Ne II] identification is warranted. It should be noted that [Ne II] is not detected in the low resolution 8–13 μm spectrum of Arp 299B1 but that the 3 σ upper limit for this feature is $2.1 \times 10^{-15} \text{ W m}^{-2}$, which is consistent with the intensity measured at high resolution. Further, the ratio of I(11.3) to I([Ne II]) (1.7) is not unusual for galaxies for which the ratio has previously been measured (RASW).

As is apparent in Table 3, while a wide range of power-law indices are necessary to describe the long-wavelength continuum, the ratio of 8.2 μm flux to model 8.2 μm flux is not significantly different from unity for a large fraction of the galaxies even in cases where the power-law index is large and a minimum near 9.7 μm is pronounced. As a result, it is not generally necessary to invoke silicate absorption to explain the observed spectra.

4 DISCUSSION

4.1 Spectral classification

RASW have found that a three-type classification scheme is sufficient to classify the 8–13 μm spectra of most galaxies. Their scheme consists of flat-featureless, silicate absorption or emission, and PAH-type (their UIR) spectra. Further, there is a general correspondence between the 8–13 μm spectrum of a galaxy and its optical spectral classification based on optical emission lines. The correspondence is that those galaxies with flat 8–13 μm spectra are often broad-line AGNs, those with silicate absorption are frequently narrow-line AGNs, and those with PAH features typically have optical spectra with line ratios similar to Galactic H II regions.

Parenthetically, the identification of the mid-infrared emission feature analysed here is not entirely secure. Other

laboratory analogs, including quenched carbonaceous composites (Sakata & Wada 1989), hydrogenated amorphous carbon (Duley 1989), and anthracite (Ellis et al. 1994), have been proposed in addition to the PAH model (Puget & Léger 1989) that is adopted here for ease of expression. However, the precise identification of the chemical source of these features is not particularly important for the present work. What is important is that the strength of one feature may be predicted to some extent from observations of another. In particular the strength of the 7.7 μm feature may be predicted from observations of the 11.3 μm feature to within about a factor of 2 (Zavagno, Cox & Baluteau 1992).

The model fitting performed at the long-wavelength end of the spectra can be used effectively to test for the presence of strong silicate absorption. Two cases might occur. First, a PAH spectrum might undergo external extinction. In this case, two effects will contribute to the model underpredicting the observed flux in the shorter wavelength half of a spectrum. The first effect is that the 11.3 μm feature will undergo more severe extinction than the region near 8 μm due to the spectral shape the silicate component of the interstellar extinction curve. This has the effect of reducing the predicted PAH strength. The second effect is that the slope of the model continuum will have a larger spectral index than would otherwise be the case if no silicate absorption were present. The model would therefore underpredict the continuum underlying the 7.7 and 8.6 μm feature complex. Both of these effects will cause the model to underpredict the shorter wavelength observations. Second, a PAH spectrum may undergo no particular extinction, however, a second silicate-absorbed continuum component may also contribute to the spectrum. In this case, the model should predict the PAH component well. However, if the silicate absorption is strong, the model spectral index will be increased due to the additional component, and the continuum in the short wavelength half will be underestimated so that the model will also underpredict the observed flux.

The RASW classification scheme is applied to the present data in the following way: the ratio of the observed to model flux density between 8.0 and 8.4 is used as a guide to classification such that if this ratio is 3 σ above 2.5, then the source is classified as silicate. This cut may somewhat underestimate the number of galaxies in which silicate absorption is present compared to the approach taken in Dudley & Wynn-Williams (1999), where the cut is taken at 2.0. For the purposes of definite classification, under the working hypothesis that all infrared galaxies are PAH-type unless convincingly shown to be otherwise, this more conservative value is appropriate. In cases where the 11.3 μm feature is not formally detected but only allowed (dot dashed curves in Fig. 1), and where a minimum is present near 9.7 μm , a question mark is appended to the PAH designation; however, whether or not there is a formal detection of the 11.3 μm feature in sources with obviously flat spectra, the classification is given as flat. A mixed classification of PAH and silicate is given where PAH emission can explain ~ 30 per cent of the observed emission between 8.0 and 8.4 μm . Under this condition, the classification of Arp 220 by RASW as both PAH and silicate would be revised to just silicate. Arp 220 is discussed in detail in Section 4.2.5.

Table 4 gives, for each source in column 1, the spectral classification based on the present data and on optical ob-

servations, along with 12–100 μm photometry, the infrared luminosity, and the star formation efficiency. In some cases the optical spectral classification has been inferred from the data of Veilleux et al. (1995), if some diagnostics were missing. It is clear from Table 4 that the general correspondence between optical spectroscopy and 8–13 μm spectroscopy is quite similar to that found by RASW. Neglecting LINER-type galaxies, four exceptions where AGNs are identified optically but which are found to have PAH-type spectra in this work are Mkn 1034, IRAS 04154+1755, IRAS 05189–2524, and Zw 475.056.

Mkn 1034 is a known Seyfert 1 galaxy; however its 8–13 μm spectrum can be fit with a PAH plus continuum model. This may be consistent with the finding of Sopp & Alexander (1992) that only half of the 6-cm flux density measured in a $14''.5$ beam is also contained within a $1''.5$ beam, suggesting that spatially extended star formation plays a role in this source. A similar explanation may be invoked for the presence of PAH emission in the spectra of the Seyfert 2 galaxies IRAS 04154+1755 and Zw 475.056. Crawford et al. (1996) find IRAS 04154+1755 to be resolved at 6 cm using both 4-arcsec and 0.5-arcsec beams. In the map of Zw 475.056 presented by CHYT, low-level radio emission extends over 1.5-arcsec. IRAS 05189–2524 is discussed in detail in the next section; however it should be noted here that the presence of exceptions, in this sample, to the the correspondence between optical and 8–13 μm spectral classification found by RASW should not be taken as evidence that the correspondence is merely coincidental. The sources presented by RASW were sometimes selected on the basis of optical spectroscopy to examine the question of what kind of spectrum they would present at 8–13 μm . Hence, many of their sources were archetypical examples of their optical class. In the present sample, selection is based solely on infrared properties, so that mixed cases might well be expected.

It is probably not coincidental that these four sources are among the sources in Table 3. with the smaller values of α suggesting that the AGN in these sources may contribute somewhat to the 8–13 μm continuum; strong 12 and 25 μm emission is known to select for AGNs that have unambiguous optical spectra (de Grijp et al. 1985; Spinoglio & Malkan, see also the AGN spectral energy distributions presented by Sanders et al. 1989).

4.2 Comments on individual ultraluminous infrared galaxies

The observed properties of the ultraluminous infrared galaxies presented here show a surprising range. A closer look at these properties will be discussed in this section.

4.2.1 A phenomenological description of IRAS 05189–2524

One of the greatest surprises in these data is the case of IRAS 05189–2524, which might have been expected to show a flat or silicate absorbed 8–13 micron spectrum based on its optical AGN-like spectrum (Sanders et al. 1988). What is observed however is a spectrum that is well fit by a PAH plus power-law continuum model (see Fig. 1). Additionally, the strength of the 11.3 μm emission relative to

the 8–1000 μm emission is quite similar to known starburst galaxies so that it seems possible that star formation might be the primary power source of the galaxy. Here, a tentative decomposition of its spectral energy distribution is proposed. In Fig. 2, a comparison is made between IRAS 05189–2524 and two known AGNs to suggest that while the 1–5 μm emission in IRAS 05189–2524 may be due to hot dust heated by an AGN, the 8–100 μm emission may be better explained as arising from star formation traced by the observed PAH emission. In Fig. 2 the power-law extrapolations of the dust continuum emission (solid lines) found in the 8–13 μm spectra are projected to 5 and 25 μm . For the two sources where the 8–13 micron emission is thought to be due to AGN-heated dust (Mkn 231 and IRAS 13349+2438) (Roche et al. 1983; Beichman et al. 1986), these extrapolations are reasonable predictors of the observed flux densities at both 5 and 25 μm . For IRAS 05189–2524 the extrapolation of the continuum to 25 μm is in reasonable agreement with the observed flux density; however the extrapolation to 5 μm fails to predict the 4–5 μm photometry of IRAS 05189–2524 (see double arrow), suggesting that an unrelated power source is responsible for this emission. Given the apparent similarity in the shape of 1–5 μm emission in both IRAS 05189–2524 and IRAS 13349+2438, it is possible that the spectral energy distribution of IRAS 05189–2524 is the result of a starburst producing the majority of the 8–100 μm emission and an AGN with a spectral energy distribution similar to that of IRAS 13349+2438 responsible for the bulk of the shorter wavelength emission but contributing little to the 8–100 μm emission. Such a decomposition could reconcile the apparently contradictory observations of both an AGN-like optical spectrum and the present PAH type 8–13 μm spectrum. A decomposition of this kind could also be consistent with the suggestion of Goldader et al. (1995) that the 2 μm continuum is dominated by AGN [heated dust] emission based on the small equivalent width of the observed Br γ emission. That hot dust typically plays a lesser role in starburst galaxies at 2 μm may also be deduced from the frequent detection of stellar continuum with probably little veiling of the CO absorption features, while in IRAS 05189–2524 CO absorption is not detected (Goldader et al. 1995). Another piece of evidence that supports the view that the AGN in IRAS 05189–2524 may not be energetically dominant is the failure to detect a radio core of extreme brightness temperature in VLBI observations (Lonsdale, et al. 1993).

The VLA radio map of CHYT shows the radio continuum in this source to be extended on a scale of 160 pc, which is comparable to the minimum blackbody diameter of 280 pc based on the observed 60 and 100 μm flux densities and assuming optically thick dust emission. It is therefore plausible that the far-infrared emission arises from optically thick warm dense clouds embedded in the starburst with a low volume filling factor but a column covering factor of order unity. The mid-infrared continuum and PAH emission present in this spectrum might arise from the surfaces of these clouds and may be optically thin in the sense that the emission arises from cloud surfaces facing our line of sight, and from a layer that is only 1–2 A_V thick on any given line of sight into the starburst.

Given the possibility of a decomposition of the 1–100 μm spectral energy distribution into a dominant star-

burst component and an AGN component important only at shorter wavelengths, the plausibility of the infrared emission being spatially associated with the radio continuum, and most importantly, the presence of 11.3 μm PAH emission in the 8–13 μm spectrum taken together with the adequate fit of the model given in Fig. 1, the 8–1000 μm emission from IRAS 05189–2524 is attributed to a starburst for the purposes of this work.

4.2.2 Digression on newly available ISO data

The model applied to the data presented in Fig. 1 for the purpose of spectral classification is not required in cases where the strength of the 7.7 μm PAH feature has been observed as is now the case for four of the ultraluminous infrared galaxies in this combined sample as a result of *Infrared Space Observatory (ISO)* observations (Genzel et al. 1998). With the additional information it is possible to compare observations with a variety of scenarios to better understand the physical situation with greater confidence than possible when only ground-based data are available. In Fig. 3, three possibilities are considered: (1) For the top spectrum in each panel, a PAH plus power-law continuum model such as that employed in Fig. 1 is fit not just in the spectral region surrounding the 11.3 μm feature, but to the entire 6–13 μm range. (2) For the middle spectrum in each panel, a PAH plus power-law continuum model is subjected to extinction by cold dust that includes the silicate absorption feature, as adopted by Dudley & Wynn-Williams (1997), and again fit to the entire 6–13 μm range. (3) For the bottom spectrum in each panel, a PAH plus power-law continuum model is additively combined with a silicate-absorbed continuum source, and again fit over the entire 6–13 μm range. The model fits presented in Fig. 3 have been carried out using CURVEFIT with equal weighting. In the first model, the index of the power-law was specified either from Table 3 (IRAS 17208–0014 and Mkn 273) or as 12.8 and 4.9 for Arp 220 and Mkn 231, respectively. It should be noted that three of the sources exhibit a large dynamic range, and in the following discussion some attention will be drawn to the poor fit at low flux density levels, which is also an expected systematic effect of the fitting procedure, since differences between small numbers are small. It may also be noted that the mismatches are apparent for a large number of neighboring data points.

4.2.3 IRAS 17208–0014

In IRAS 17208–0014, all models give fairly adequate fits to the data, and deciding between them depends mainly on other observational evidence. The strongest evidence that supports a preference for the fit shown for the top spectrum is that this source is extended on a scale ~ 1.7 kpc in the radio (Condon et al. 1996), although higher spatial resolution observations reveal the presence of a sub-kpc radio continuum source associated with the OH maser emission (Martin et al. 1989). The failure of Martin et al. (1989) to detect more extended emission may be due to the restricted set of base lines they employed. When this evidence is taken along with the optical spectral classification of Veilleux et

al. (1995) in which the line ratios in this source are similar to those in H II regions, there is no strong reason to suspect that anything other than star formation is responsible for the observed mid-infrared spectrum. Nor is there any reason to suspect a high degree of extinction; IRAS 17208–0014 is among the sources presented by Genzel et al. (1998) for which the continuum underlying the 12.8- μm [Ne II] feature in their SWS data can be comfortably plotted on the scale of the ISOPHOT-S data in their fig. 2, suggesting a lack of strong silicate absorption (see also Fig. 1). The fit to the upper spectrum might be improved somewhat by increasing the strength of the 7.7 and 6.2 μm features by a factor of 2, a procedure which is probably allowed for the 7.7 μm feature at least since the Orion Bar spectrum used as a template here is known to have a somewhat weaker than usual 7.7 μm feature relative to the 11.3 μm feature (Zavagno et al. 1992).

4.2.4 Mkn 273

The fit to the top spectrum of Fig. 3 for Mkn 273 gives, as might have been anticipated from Fig. 1, a poor representation of the data. The fitted strength of the 11.3 μm feature is clearly too large, which is roughly the converse of the result in Fig. 1. Thus, it may be concluded that a simple PAH plus power-law continuum model does not describe these data. The fit shown for the middle spectrum is better, in that it requires less PAH emission over all and the strength of the 11.3 μm feature is not over-predicted; however the continuum around the 9.7 μm silicate minimum is not well reproduced. This suggests that an unaccounted-for emission component is required to produce this emission. The fit to the lower spectrum overcomes this difficulty by superimposing an unobscured PAH plus power-law continuum such as that which fit IRAS 17208–0014 (top spectrum) upon a continuum source that suffers strong silicate absorption. Since Mkn 273 shows clear signs of nuclear activity (Armus, Heckman & Miley 1989; Veilleux et al. 1995), a silicate-absorbed continuum source might be produced by an edge-on view of a disk model such as those proposed by Pier & Krolik (1992) or Efstathiou & Rowan-Robinson (1995), which are natural elaborations of the AGN unification model proposed by Antonucci & Miller (1985). The continuum level evident in the SWS observations of 12.8- μm [Ne II] in Genzel et al. (1998) is consistent with the new CGS3 data presented here; and therefore consistent with silicate absorption playing a role in this source. If the fit to the bottom spectrum is accepted, then the AGN component could well be responsible for the greater fraction of the 60 and 100 μm emission.

4.2.5 Arp 220

Prior to the new *ISO* observations the analysis of the Arp 220 spectrum would have proceeded very much along the lines that have just been given for Mkn 273 (Smith et al. 1989), with the proviso that Arp 220 has less obvious signs of activity in its nucleus so that disk-like models for the silicate-absorbed continuum emission may be less helpful in advancing our understanding, and deeply embedded models perhaps more descriptive (Dudley & Wynn-Williams 1997). Applying the model used in Fig. 1 to the data of Smith et

al. (1989) severely under-predicts the observed $8.2 \mu\text{m}$ flux density. However, as can be seen in Fig. 3 the new *ISO* data can apparently be fit by a simple PAH plus power-law continuum model due to the apparent discrepancy between the observations of the $11.3 \mu\text{m}$ feature reported by Smith et al. (1989) and the *ISO* data of Genzel et al. (1998). It should be noted that there are no continuum points longward of the $11.3 \mu\text{m}$ feature in the new *ISO* data, so that determining its strength from those data is difficult. It seems safer at this point to accept the ground-based data as a guide in this spectral region and thus hold this model in abeyance, pending further observational evidence. The fit to the middle spectrum is essentially the same as that given in fig. 1 of Smith et al. (1989) and suffers from the same difficulty noted by Smith et al. (1989), namely that the minimum near $9.7 \mu\text{m}$ is poorly fit. The fit to the lower plot is similar to that shown in Smith et al.'s (1989) fig. 2 or as adopted by Dudley & Wynn-Williams (1997). The continuum in the $12.8\text{-}\mu\text{m}$ [Ne II] SWS data of Genzel et al. (1998) is consistent with the Smith et al. (1989) data but is not apparently consistent with the ISOCAM-CVF spectrum presented by Elbaz et al. (1998).

For Arp 220, therefore, the new *ISO* data presented by Genzel et al. (1998) seems to allow the possibility that unextinguished PAH emission plus a simple power-law continuum describes this spectrum as a result of the apparent strength of the $11.3 \mu\text{m}$ feature in the new data. It has been suggested that differing spectral resolution (roughly a factor of 2) between the Smith et al. (1989) and Genzel et al. (1998) data may account for this difference, however this could only work and if the $11.3 \mu\text{m}$ feature were unresolved in both spectra, and that does not appear to be the case. Gauging the overall PAH emission from the $6.2 \mu\text{m}$ feature which displays continuum on either side, the intensity of which is found to be well correlated with the that of the $7.7 \mu\text{m}$ feature in Galactic sources (Cohen et al. 1989), it is clear the PAH emission relative to the over-all $8\text{--}1000 \mu\text{m}$ emission is exceedingly weak, really no stronger than what might be allowed in Mkn 231 (see next), if the apparent $6.2 \mu\text{m}$ feature in the *ISO* data for Mkn 231 is real. In contrast, again using the $6.2 \mu\text{m}$ PAH feature as a guide, the strength of the PAH emission relative to the $8\text{--}1000 \mu\text{m}$ emission in Mkn 273 is twice as strong, and in IRAS 17208–0014, five times as strong. The Arp 220 spectrum might possibly be produced by a starburst that reprocesses more than 90 per cent of its luminosity not once but many times so that the observed PAH emission is produced only in a thin outer shell or in a small number of narrow chinks. Such a model would be even more extreme than what is argued above as plausible for IRAS 05189–2524 in a starburst context. However, given the disagreement between the two spectra of this source near $11.3 \mu\text{m}$ and in consideration of the arguments of Dudley & Wynn-Williams (1997), a model that has both unobscured PAH emission and a silicate-absorbed continuum due to a deeply embedded AGN continues to seem more natural. This interpretation also seems to account simultaneously for both the $158\text{-}\mu\text{m}$ [CII] (Luhman et al. 1998) and 2–10 keV X-ray (Iwasawa 1999) deficits in this source if the “AGNs” (Soifer et al. 1999) are sufficiently obscured. It should be noted that in this preferred model, only a fraction of the flux density at $7.7 \mu\text{m}$ can be attributed to the $7.7 \mu\text{m}$ PAH feature, in accordance with either the 12.8 or $14.3 \mu\text{m}$ continuum

seen in the SWS data presented by Genzel et al. (1998). As suggested by Dudley & Wynn-Williams (1997), spatially resolved spectroscopic observations may help to clarify this issue.

4.2.6 Mkn 231

For Mkn 231 any PAH contribution to the spectrum must be minimal compared to a continuum contribution (Roche et al. 1983), as can also be seen from the fit to the upper spectrum in Fig. 3. This source had been fit adequately with a model consisting of a continuum source suffering silicate absorption by Roche et al. (1983), and the present models are *not* an improvement. It would be of interest to know if disk radiative transfer models such as those proposed by Pier and Krolik (1992) would fair as well as the cold absorber model of Roche et al. (1983) in the detailed fit to the silicate absorption feature given their likely success in fitting the overall infrared spectral energy distribution of Mkn 231. The $11.3 \mu\text{m}$ emission feature is not detected in this source and it is not clear that the single point that is spectrally coincident with the $6.2 \mu\text{m}$ feature in the *ISO* data should be considered as a real indication of the presence of PAH emission. Some PAH emission is not unexpected in this source given the presence of star-forming knots near the nucleus of this source that might account for ~ 10 per cent of its infrared luminosity (Surace et al. 1998). The estimate of the $7.7 \mu\text{m}$ PAH strength given by Genzel et al. (1998) relies on a continuum point at $10.9 \mu\text{m}$ which lies in the silicate absorption feature. Of the sources measured in this way by Genzel et al. (1998) Mkn 231 perhaps provides the clearest example of how this method is prone to overestimate the PAH strength when silicate absorption is present. The 12.8 or $14.3 \mu\text{m}$ continuum in their fig. 1 provide a rough guide as to when there may be a problem in this respect. For Mkn 231, the $12.8 \mu\text{m}$ continuum of Genzel et al. (1998) is high in comparison with the data of Roche et al. (1983) but it is possible that it would agree with the extrapolation of the long-wavelength ISOPHOT-S data which also apparently fall significantly above the Roche et al. (1983) data as seen in Fig. 3. It is not clear if these differences should be attributed to aperture effects, or other systematics, or if they reflect intrinsic source variability over 1.4 decade; Roche et al. (1983) found good agreement with the narrowband photometric observations of Reike (1976) made over 0.4 decade earlier.

4.3 A $60 \mu\text{m}$ flux-limited subsample

Among galaxies with $L_{\text{IR}} \geq 1.6 \times 10^{11} L_{\odot}$, a nearly complete (all but three sources have $8\text{--}13 \mu\text{m}$ spectra) flux-limited (at $60 \mu\text{m}$) sample of 25 sources may now be defined on the combined Bright Galaxy Survey (Soifer et al. 1989) and the Extended Bright Galaxy Survey (Sanders et al. 1995) (combined BGS) for $F_{\nu}(60) \geq 11.25$ Jy (roughly twice the flux limit of combined BGS). The only other restriction on this subsample is that the sources be observable using UKIRT, i.e. $-25^{\circ} \leq \delta \leq 60^{\circ}$. Table 5 gives the ultraluminous and luminous samples with the source name in column 1, the $8\text{--}13 \mu\text{m}$ spectral classification in column 2, the reference for the $8\text{--}13 \mu\text{m}$ spectrum in column 3, the log of the $8\text{--}1000$

μm luminosity in column 4, and the log of the ratio of the 12 μm flux density to the 60 μm flux density in column 5. The ultraluminous sample has 5 members and the luminous comparison sample has 20 members. The ultraluminous sample is *unlikely* to span all the possible characteristics of ultraluminous infrared galaxies and therefore is not fully representative. There are two observations that confirm this: (1) if Arp 220 were scaled to the 60 μm 11.25 Jy flux limit used to define this sample, it would not have been observable using CGS3 or other ground-based spectrographs available when these data were collected, and (2) the ratio given in column 5 of Table 5 for the two brightest ultraluminous galaxies (Arp 220 and Mkn 231) bracket the same ratio for all the galaxies in the sample with $1.6 \times 10^{11} \leq L_{\text{IR}} \leq 10^{12} L_{\odot}$ except NGC 1068 and NGC 7469. An analysis over the entire Bright Galaxy Survey shows that the dispersion of this ratio is indeed larger for ultraluminous infrared galaxies than for luminous infrared galaxies by a factor of 2 (Soifer & Neugebauer 1991). Thus, conclusions based on the present flux-limited sample of ultraluminous galaxies should be viewed with caution not simply because of the small number of galaxies in this sample (counting statistics on a bimodal parent population), but because the characteristics of the parent population are not well represented (under-sampling).

It is possible that the last of these two difficulties could be somewhat ameliorated by the following considerations. Ultraluminous galaxies that fall outside the range of 12 on 60 μm flux density ratios defined by Arp 220 and Mkn 231 may be assigned to the AGN-dominated bin in the context of exploring the AGN vs. starburst hypotheses. For ultraluminous galaxies with 12/60 μm colors redder than Arp 220, PAH emission cannot make a contribution to the 12 μm flux density that is sufficiently large to explain the 60 μm flux density. It is therefore likely that such sources will have deep silicate absorption features, and by the arguments presented by Dudley & Wynn-Williams (1997), the size of their power source should be too small to be due to a starburst. For galaxies with 12/60 μm colors bluer than Mkn 231, 60 μm selected samples will overlap 25 or 12 μm selected samples that are known to select for AGNs (de Grijp et al. 1985; Spinoglio & Malkan 1989). However, reliance on these notions would be ill advised given the internal evidence in the present data showing that PAH emission can be important in ultraluminous galaxies with 12 to 60 μm flux density ratios similar to the two extremes, namely, IRAS 17208–0014 and IRAS 05189–2524.

Inspection of Table 5 shows that 3 out of 5 of the ultraluminous galaxies are powered predominantly by AGNs although if judgment is reserved for Arp 220, this fraction would be 2 out of 5. The trend is thus consistent with about half of ultraluminous galaxies being powered by AGNs. On the other hand, the fraction of the more numerous luminous galaxies in this sample that are powered predominantly by AGNs is at most 0.25 and could be as small as 0.05 or smaller if the relative contributions of the AGN and starburst in NGC 1068 are approximately equal (Telesco et al. 1984). This trend supports the evidence from optical spectroscopy that AGNs are present in greater numbers in ultraluminous infrared galaxies (Veilleux et al. 1995). It goes further than optical or radio studies because it is possible to demonstrate with greater certainty which type of power source (starburst or AGN) dominates the infrared luminosity. Further, it is

apparent that for luminosities less than $10^{12} L_{\odot}$, star formation is far and away the dominant power source, a result that confirms work at many wavelengths. This analysis lends some support to the proposal of Sanders et al. (1988) that there is an evolutionary connection between ultraluminous infrared galaxies and quasars, while at the same time demonstrating that massive star formation can indeed be the dominant power source of some ultraluminous infrared galaxies. However, it must be conceded that the evidence presented constitutes only a trend. The precise proportion of AGN-dominated sources among 60 μm selected ultraluminous infrared galaxies cannot be said to have been established here, and thus no statistically meaningful difference between luminous and ultraluminous galaxies has truly been shown. It is of interest that the trend does continue with the next step down in 60 μm flux density. Adding IRAS 12112+0305 and IRAS 08572+3915 to the present sample of five ultraluminous galaxies adds one apparently starburst-dominated (based on the apparently normal ratio of the 6.2 μm PAH feature emission to overall infrared emission in the IRAS 12112+0305 spectrum of Genzel et al. 1998[†]) and one AGN-dominated object (Dudley & Wynn-Williams 1997).

4.4 Anti-correlation between 11.3 μm equivalent width and $L_{\text{IR}}/M(\text{H}_2)$

In Fig. 4 a possible anti-correlation between the equivalent width (EW) of the 11.3 μm feature and the global ratio of $L_{\text{IR}}/M(\text{H}_2)$ is presented for a number of galaxies. The EW data are based either on the model fits given in Table 3 or the previously published values of RASW reproduced in Table 6. The ratios of infrared luminosity to H_2 mass are taken from the literature (Tables 4 and 6). The solid line in Fig. 4 indicates inverse proportionality.

The ratio $\frac{L_{\text{IR}}}{M(\text{H}_2)}$ is often taken to be a measure of star formation efficiency. When it is large, then a large fraction of the available gas is involved in star formation; when it is small, conditions may be such that the gas exists in a more quiescent state. However, for a very large ratio of $\frac{L_{\text{IR}}}{M(\text{H}_2)}$, Sanders et al. (1991) argued that even a very high star formation efficiency cannot account for the infrared luminosity, on the grounds that star formation would too quickly consume the available gas mass, so that AGN-like activity might be the more likely primary power source of the infrared luminosity. Both $\frac{L_{\text{IR}}}{M(\text{H}_2)}$ and EW(11.3) are independent of distance in so far as EW(11.3) is independent of aperture size.

A tendency for EW(11.3) to be anti-correlated with the star formation efficiency might arise if two conditions were met. First, if the intensity of the 11.3 μm feature is a roughly constant fraction of the overall infrared emission (proportional to L_{IR}) then this will not contribute to the anti-correlation. Second, if the strength of the continuum at 11.3 μm increases with decreasing availability of dust (inversely proportional to $M(\text{H}_2)$) to reprocess the light emitted by massive stars so that a larger fraction of the dust

[†] A crude attempt to correct for the contribution of the silicate absorption edge to the 7.7 μm PAH feature by fitting a power law to continuum points at 5.9 and 14.3 μm suggests a deficit in the strength of the 7.7 μm feature for IRAS 12112+0305.

grain population is heated to the warm temperatures required for the dust grains to emit at $11.3\ \mu\text{m}$ then this could be the source of anti-correlation. Such an explanation requires further elaboration since the process by which the $11.3\ \mu\text{m}$ continuum is produced is likely, in general, to be a local phenomenon rather than a global one.

An elaboration that may be in keeping with recent *HST* observations (Watson et al. 1996; Surace et al. 1998; Satyapal et al. 1997) is that as the star formation efficiency increases, the proportion of massive stars formed in dense clusters may increase. If this is the case, then the time-scale for clearing the interstellar medium from around these clusters to a distance where dust grains would no longer be heated sufficiently to contribute to the $11.3\ \mu\text{m}$ continuum may be longer than the time-scale for clearing the interstellar medium around the groups of massive stars that might form if the star formation efficiency is lower. Two effects may contribute to this. First, the distance at which a grain could be heated to a temperature high enough to contribute to the $11.3\ \mu\text{m}$ continuum would increase as the square root of the number of massive stars in a cluster so that if the velocity of gas and dust being cleared from clusters of massive stars is not too different from the velocity of gas and dust cleared from groups of massive stars, the dust remains heated for a longer period of time. Second, dense clusters might be temporarily gravitationally bound and behave ballistically with respect to the dissipative gas. They may sometimes move into a fresh reservoir of gas, heating the associated dust to higher temperatures.

In this view, the additional contribution to the $11.3\ \mu\text{m}$ continuum emission at higher star formation efficiency would be provided by possibly equilibrium temperature grains heated by a combination of direct and Ly α heating rather than small grains heated by a single photon. To zeroth order, this is a sensible proposition, since one expects (at least within photo-dissociation regions) that the PAH emission and the spike-heated grain emission to have roughly fixed relative contributions at $11.3\ \mu\text{m}$ due to the rough similarity of the emission time scales for the two emission processes, so that the apparent anti-correlation would not necessarily arise.

A number of observations will be required to examine this situation. Most important are higher signal-to-noise observations that will allow real measurements of EW(11.3) for a number of the sources included in Fig. 4. These are required to decide if the anti-correlation is has any merit. Another avenue of investigation would be to make higher spatial resolution observations of nearby starbursts where clusters of massive stars are observed to exist to establish whether or not EW(11.3) does decrease in the vicinity of some clusters (see Dudley & Wynn-Williams 1999 for a preliminary attempt). Finally, high spatial resolution $2\ \mu\text{m}$ adaptive optics imaging of a number of starbursts with a range of star formation efficiency can help to determine if the fraction of massive stars that exist in dense clusters varies with the star formation efficiency parameter as conjectured here.

5 CONCLUSIONS

New 8–13 μm spectroscopy of 27 infrared galaxies has been presented. The spectra have been fit with a two-component model consisting of a power-law continuum underlying a PAH emission spectrum. These fits are based on the spectral data between 10 and 13 μm and are used to predict the flux emitted between 8.0 and 8.4 μm . It is found that for the majority of the observed galaxies, the model predicts the observed 8.0–8.4 μm emission to within an acceptable factor of 2, suggesting that the majority of the sources are powered by starbursts.

One source, Mkn 273, has been found to show very clear evidence for silicate absorption.

A flux-limited 60 μm selected subsample that combines the present spectroscopic results and those of RASW had been defined, consisting of 25 galaxies. In this subsample the fraction of ultraluminous infrared galaxies powered by AGN is ~ 50 per cent in contrast to 5–25% among the luminous infrared galaxies. Owing to the small sample size for the ultraluminous infrared galaxies, this difference in AGN fraction can be considered only a trend.

A possible anti-correlation is identified between the equivalent width of the $11.3\ \mu\text{m}$ PAH feature and the star formation efficiency in galaxies where both have been measured. It is suggested that variation in the continuum dust temperature as a function of star formation efficiency could produce this apparent effect.

ACKNOWLEDGMENTS

The author would like to thank the UKIRT staff: Joel Aikock, Tim Caroll, Dolores Walthers, and Thor Wold, for assistance at the telescope, and John Davies, Tom Geballe, and Gillian Wright for fruitful discussions and calibration data in advance of publication. UKIRT is operated by the Joint Astronomy Centre on behalf of the U. K. Particle Physics and Astronomy Research Council. Brian Rush, Reinhart Genzel, Vassilis Chamanadaris, Joe Hora, and D.-C. Kim all kindly provided data in advance of publication. A series of exchanges with Dieter Lutz has help to clarify certain issues, as has a discussion with Gary Neugebauer, Keith Matthews and Eichi Egami. Eric Becklin has provided thoughtful comments at several stages of this work. Many members of the Institute for Astronomy have benefited this work through discussion and sharing of work in progress. A few are Gareth Wynn-Williams (dissertation committee chair), Dave Sanders, Bob Joseph, Klaus Hoddap, Josh Barnes, Alan Tokunaga, Jeff Goldader, Jason Surace, and Masatoshi Imanishi; thanks are due to these and others. Louise Good proofread the manuscript prior to submission. This work has been partially supported by NSF grants ASTR-8919563, NASA grant NAGW-3938, and the Frank Orrall fund. The NASA Extragalactic Database (NED) has been a constant aid. It is run by the Jet Propulsion Laboratory, California Institute of Technology, under contract with NASA. This work has also made use of NASA's Astrophysics Data System Abstract Service.

REFERENCES

- Antonucci R. R. J., Miller J. S., 1985, *ApJ*, 297, 621
- Armus L., Heckman T. M., Miley G. K., 1989, *ApJ*, 347, 727
- Beichman C. A., Soifer B. T., Helou G., Chester T. J., Neugebauer G., Gillett F. C., Low F. I., 1986, *ApJ*, 308, L1
- Bevington P. R., 1969, *Data Reduction and Error Analysis for the Physical Sciences*. McGraw-Hill, New York
- Clements E. D., 1981, *MNRAS*, 197, 829
- Cohen, M., Tielens, A. G. G. M., Bregman, J., Witteborn, F. C., Rank, D. M., Allamandola, L. J., Wooden, D. H., de Muizon, M., 1989, *ApJ*, 341, 246
- Cohen M., Davies J. K., 1995, *MNRAS*, 276, 715
- Cohen M., Witteborn F. C., Walker R. G., Bregman J. D., Wooden D. A., 1995, *AJ*, 110, 275
- Condon J. J., Helou G., Sanders D. B., Soifer B. T., 1990, *ApJS*, 73, 359
- Condon J. J., Huang Z.-P., Yin Q. F., Thuan T. X., 1991, *ApJ*, 378, 65 (CHYT)
- Condon J. J., Frayer D. T., Broderick J. J., 1991, *AJ*, 101, 362
- Condon J. J., Helou G., Sanders D. B., Soifer B. T., 1996, *ApJS*, 103, 81
- Crawford, T., Marr, J., Partridge, B., Strauss, M. A., 1996, *ApJ*, 460, 255
- de Grijp M. H. K., Miley G. K., Lub J., De Jong T., 1985, *Nature*, 314, 240
- Dudley C. C., 1998, PhD thesis, Univ. Hawaii
- Dudley C. C., Wynn-Williams C. G., 1993, *ApJ*, 407, L68
- Dudley C. C., Wynn-Williams C. G., 1997, *ApJ*, 488, 720
- Dudley C. C., Wynn-Williams C. G., 1999, *MNRAS*, in press
- Duley W. W., 1989, in Allamandola L. J., Tielens A. G. G. M., eds, *Proc. IAU Symp. 135, Interstellar Dust*. Kluwer, Dordrecht, p. 141
- Eales S. A., Becklin E. E., Hodapp K.-W., Simons D. A., Wynn-Williams C. G., 1990, *ApJ*, 365, 478
- Efstathiou A., Rowan-Robinson M., 1995, *MNRAS*, 273, 649
- Elbaz, D., et al., 1998, in Cox, P. Kessler, M. F., eds, *The Universe as seen by ISO*, UNESCO, Paris, ESA, SP-427, in press, (astro-ph/9902229)
- Ellis K., Guillois O., Nenner I., Papoular R., Reynard C., 1994, in Nenner, I., ed, *Molecules and Grains in Space*. Amer. Inst. Phys., New York, p. 811
- Genzel R. et al., 1998, *ApJ*, 498, 579
- Goldader J. D., Joseph R. D., Doyon R., Sanders D. B., 1995, *ApJ*, 444, 97
- Hanner M. S., Brooke T. Y., Tokunaga A. T., 1995, *ApJ*, 438, 250
- Hewitt A., Burbidge G., 1989, *ApJS*, 69, 1
- Helou, G., Soifer, B. T., Rowan-Robinson, M., 1985, *ApJ*, 298, L7
- Horellou C., Casoli F., Combes F., Dupraz C., 1995, *A&A*, 298, 743
- Iwasawa, K., 1999, *MNRAS*, 302, 96
- Joseph R. D., Wright G. S., 1985, *MNRAS*, 214, 87
- Joy M., Lester D. F., Harvey P. M., Telesco C. M., Decher R., Rickard L. J., Bushouse H., 1989, *ApJ*, 339, 100
- Keel W. C., Windhorst R. A., 1991, *ApJ*, 383, 135
- Keto E. et al., 1997, *ApJ*, 485, 598
- Krügel E., Steppe H., Chini R., 1990, *A&A*, 299, 17
- Lonsdale C. J., Smith H. E., Lonsdale C. J., 1993, *ApJ*, 405, L9
- Luhman, M. L., et al., 1998, *ApJ*, 504, L11
- McAlary C. W., McLaren R. A., Crabtree D. R., 1979, *ApJ*, 237, 471
- Martin, J. M., Bottinelli, L., Dennefeld, M., Gouguenheim, L., Le Squeren, A. M., 1989, *A&A*, 208, 39
- Mazzarella J. M., Balzano V. A., 1986, *ApJS*, 62, 751
- Mazzarella J. M., Boroson T. A., 1993, *ApJS*, 85, 27
- Mirabel I. F., Booth R. S., Johansson L. E. B., Garay G., Sanders D. B., 1990, *A&A*, 236, 327
- Moshir M. et al., 1990, *IRAS Faint Source Catalog*, ver. 2
- Perez E., Manchado A., Garcia-Lario P., Pottasch S. R., 1990, *A&A*, 227, 407
- Pier E. A., Krolik J. H., 1992, *ApJ*, 401, 99
- Puget L. J., Léger A., 1989, *ARA&A*, 27, 161
- Reike, G. H., 1976, *ApJ*, 210, L5
- Roche P. F., 1989, in Kaldeich B. A., ed, *Proc. 22 Eslab Symposium on Infrared Spectroscopy in Astronomy*. ESA, Paris, p. 79
- Roche P. F., Aitken D. K., Whitmore B., 1983, *MNRAS*, 205, 21P
- Roche P. F., Aitken D. K., Smith C. H., 1989, *MNRAS*, 236, 485
- Roche P. F., Aitken D. K., Smith C. H., Ward M. J., 1991, *MNRAS*, 248, 606, (RASW)
- Rush B., Malkan M., Spinoglio L., 1993, *ApJS*, 89, 1
- Sakata A., Wada S., 1989, in Allamandola L. J., Tielens A. G. G. M., eds, *Proc. IAU Symp. 135, Interstellar Dust*. Kluwer, Dordrecht, p. 191
- Sanders D. B., Soifer B. T., Elias J. H., Madore B. F., Matthews K., Neugebauer G., Scoville N. Z., 1988, *ApJ*, 325, 74
- Sanders, D. B., Phinney, E. S., Neugebauer G., Soifer B. T., Matthews K., 1989, *ApJ*, 347, 29
- Sanders D. B., Scoville N. Z., & Soifer B. T., 1991, *ApJ*, 370, 158
- Sanders D. B., Egami E., Lipari S., Mirabel I. F., Soifer B. T., 1995, *AJ*, 110, 1993
- Sargent A., Scoville N. Z., 1991, *ApJ*, 366, L1
- Satyapal S., Watson D. M., Pipher J. L., Forrest W. J., Greenhouse M. A., Smith H. A., Fischer J., Woodward C. E., 1997, *ApJ*, 483, 148
- Smith C. H., Aitken D. K., Roche P. F., 1989, *MNRAS*, 241, 425
- Smith H. E., Lonsdale C. J., Lonsdale C. J., 1998, *ApJ*, 492, 137
- Soifer B. T., Neugebauer G., 1991, *AJ*, 101, 354
- Soifer B. T., Boehmer L., Neugebauer G., Sanders D. B., 1989, *AJ*, 98, 766
- Soifer, B. T., Neugebauer, G., Matthews, K., Becklin, E. E., Ressler, M., Werner, M. W., Weinberger, A. J., Egami, E. E., 1999, *ApJ*, in press (astro-ph/9810120)
- Solomon P. M., Sage L. J., 1988, *ApJ*, 334, 613
- Solomon P. M., Downes D., Radford S. J. E., Barrett J. W., 1997, *ApJ*, 478, 144
- Sopp H., Alexander P., 1992, *MNRAS*, 259, 425
- Spinoglio L., Malkan M. A., 1989, *ApJ*, 342, 83
- Strauss M. A., Huchra J. P., Davis M., Yahil A., Fisher K. B., Tonry J., 1992, *ApJS*, 83, 29
- Surace J. A., Sanders D. B., Vacca W. D., Veilleux, S., Mazzarella J. M., 1998, *ApJ*, 492, 116
- Telesco C. M., Becklin E. E., Wynn-Williams C. G., Harper D. A., 1984, *ApJ*, 282, 427
- Veilleux S., Kim D.-C., Sanders D. B., Mazzarella J. M., Soifer B. T., 1995, *ApJS*, 98, 171
- Watson A. M., et al., 1996, *AJ*, 112, 534
- Wynn-Williams C. G., Eales S. A., Becklin E. E., Hodapp K.-W., Joseph R. D., McLean I. S., Simons D. A., Wright G. S., 1991, *ApJ*, 377, 426
- Zavagno A., Cox P., Baluteau J. P., 1992, *A&A*, 259, 241

Figures for 8–13 μm spectroscopy of luminous and ultraluminous infrared galaxies

C. C. Dudley

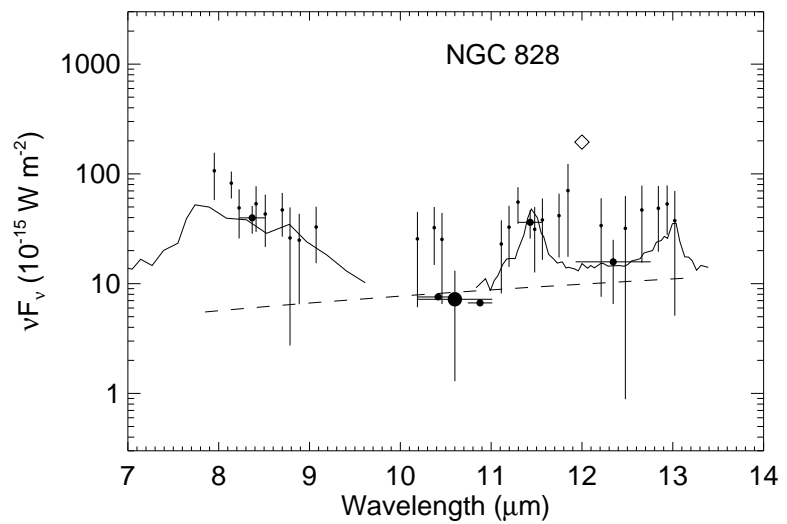
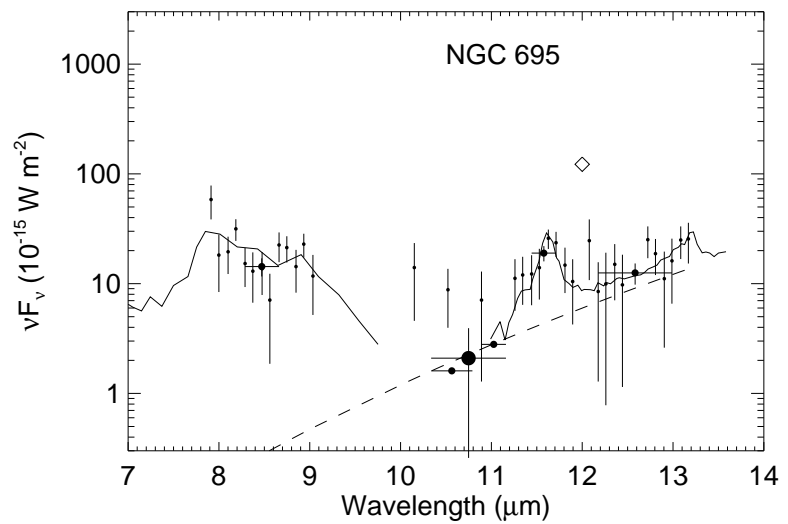
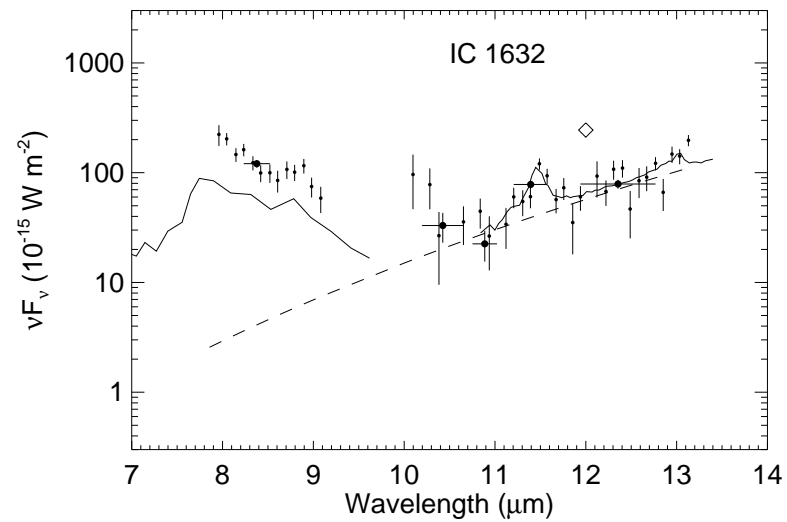
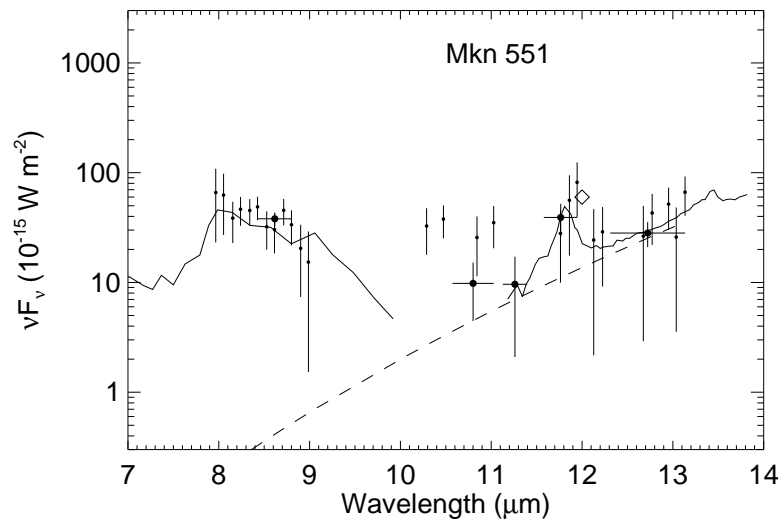
Institute for Astronomy, 2680 Woodlawn Dr., Honolulu, Hawaii 96822, USA

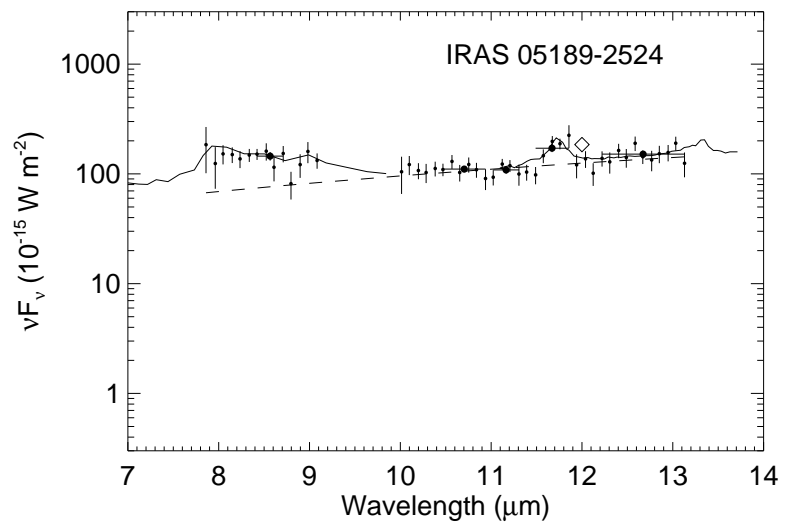
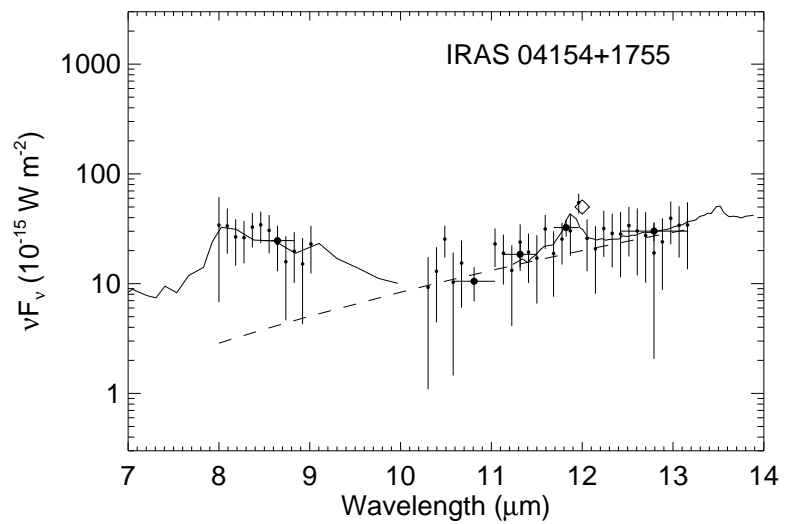
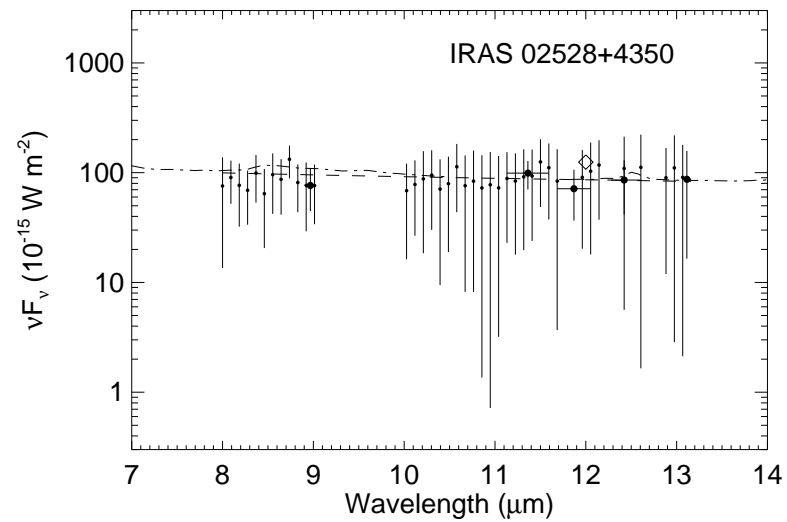
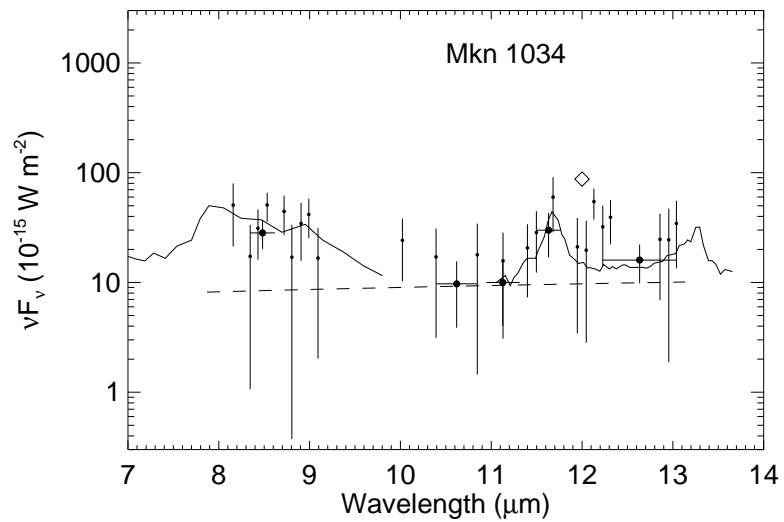
Figure 1. 8–13 μm spectra of 27 galaxies are presented. The small filled circles are the (nearly) independent data points discussed in Section 2.1 with 1σ error bars. The filled circles, which are either twice as large or four times as large as the spectral data, are the same data binned over the ranges indicated by the horizontal bars. The largest of these filled circles are shown only when one or both of the rest wavelength bins, 10–10.5 or 10.5–10.9 μm , represent detections of $<1\sigma$ significance. Apparent differences between the spectral and binned data are due to missing spectral data points that, by themselves, are upper limits only. The dashed lines represent the best-fitting power-law long-wavelength continuum underlying a PAH spectrum of the Orion Bar represented by solid or dot-dashed lines. Dot dashed lines are used when the formal uncertainty in the strength of the fitted PAH component is more than three times greater than the fitted strength of the component and are shown at the formal 3σ upper limit to the strength PAH component. Diamonds represent IRAS 12 μm fluxes, the sources of which are given in Table 4. For Arp 299B1, the high-resolution spectrum is also presented in the figure divided by a factor of 10 for clarity.

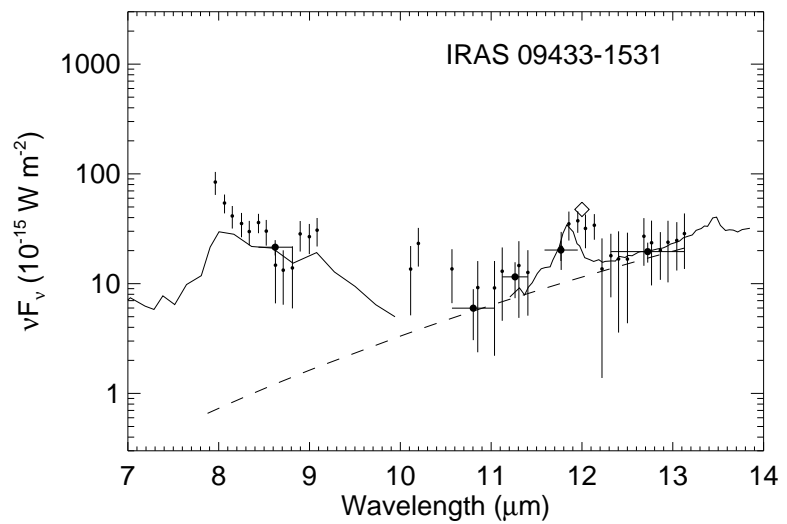
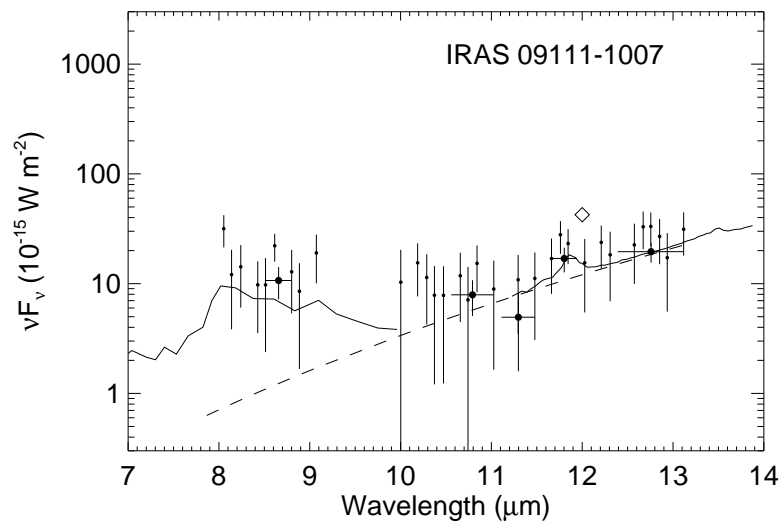
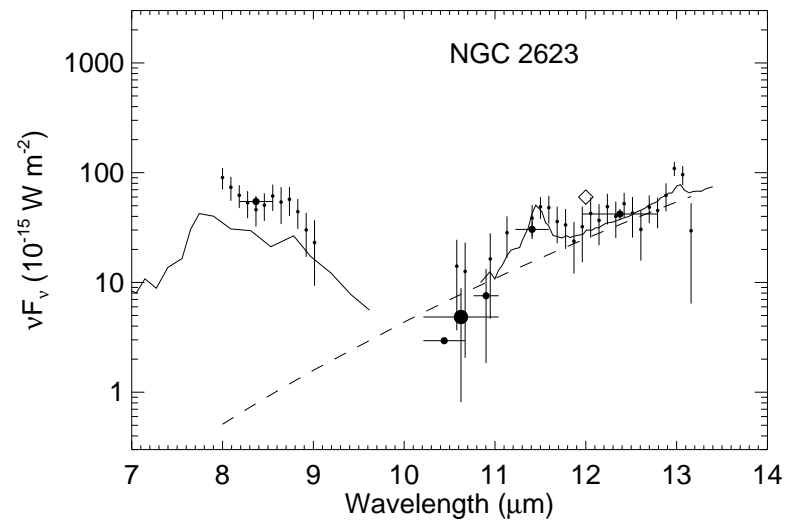
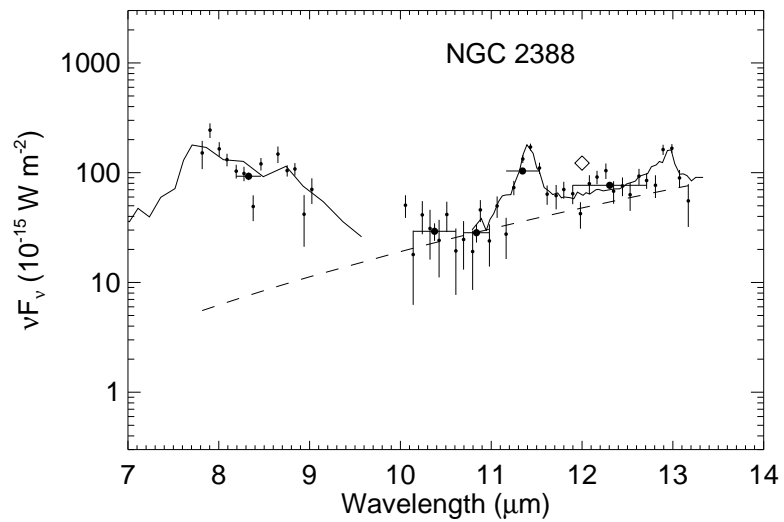
Figure 2. The spectral energy distribution of IRAS 05189–2524 is compared with those of another ultraluminous infrared galaxy: Mkn 231 and the infrared loud quasar IRAS 13349+2438. In the figure, 0.9–5 μm photometry (open diamonds) are from McAlary, McLaren & Crabtree (1979) for Mkn 321; from Dudley (1998) for IRAS 05189–2524 with the exception of the 0.9 μm point which, is from Surace et al. (1998); and from Beichman et al. (1986) for IRAS 13349+2438 (including the IRAS data). 8–13 μm spectroscopy (filled circles) is from Roche, Aitken & Whitmore (1983) for Mkn 231 and from this work for the remaining two sources. IRAS data are given by open squares. The data for IRAS 13349+2438 have been presented in the quasar's rest frame, and the spectral energy distributions of IRAS 05189–2524 and IRAS 13349+2438 have been divided by factors of 2 and 20, respectively.

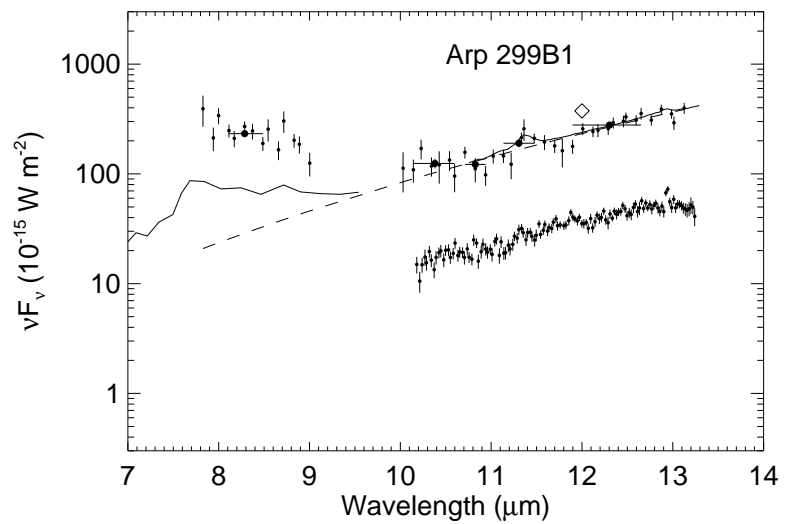
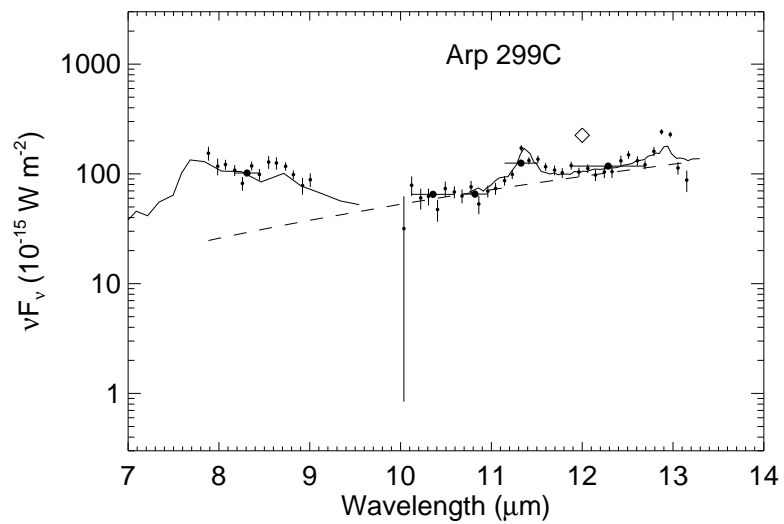
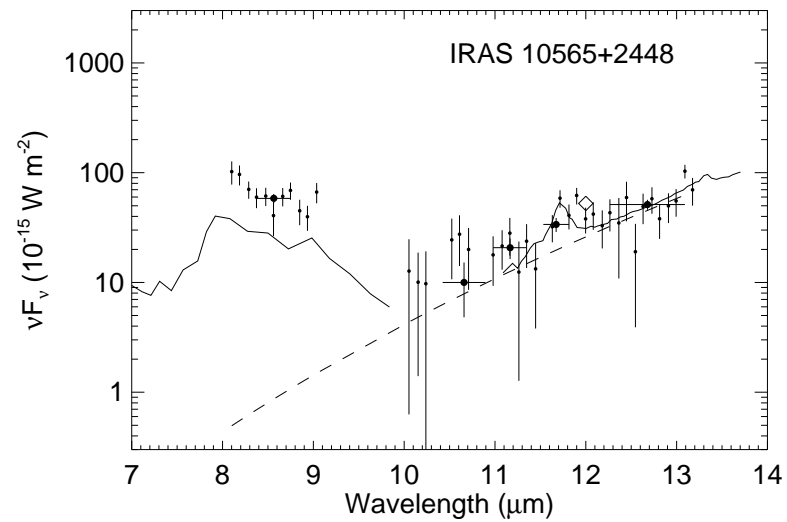
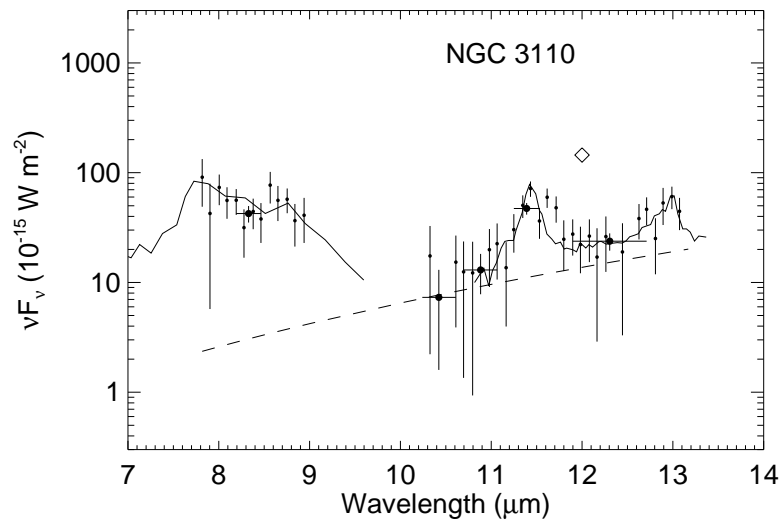
Figure 3. The combined ground-based and *ISO* spectra of four ultraluminous galaxies are presented in the observed frame. For each galaxy, the top spectrum gives the observed spectrum, while the lower two are shifted by multiplicative factors. The ground based data (filled circles) are from this work for IRAS 17208–0014 and Mkn 273, from Smith et al. (1989) for Arp 220, and from Roche et al. (1983) for Mkn 231. The *ISO* data (open circles) are from Genzel et al. (1998) and have been corrected by a factor of 1.4. Three dust emission models are shown for each source with the total emission given by the solid lines and continuum emission given by the broken lines; for the fits to the bottom spectra, an additional unobscured power-law continuum component is not shown.

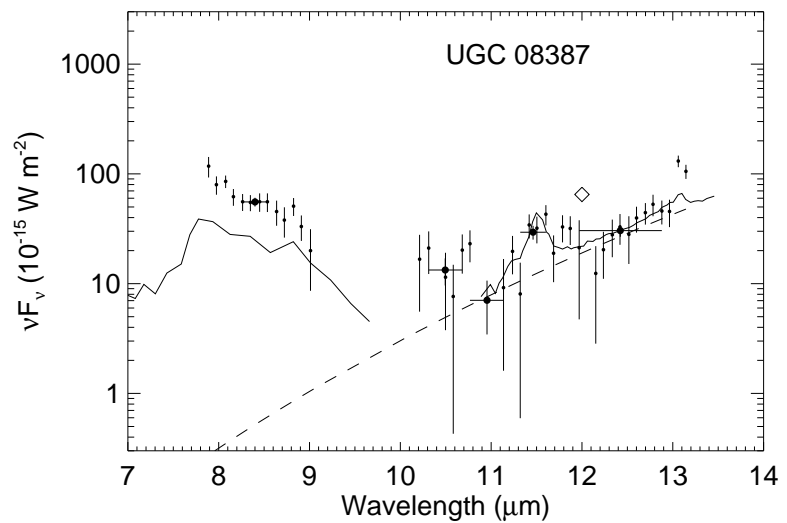
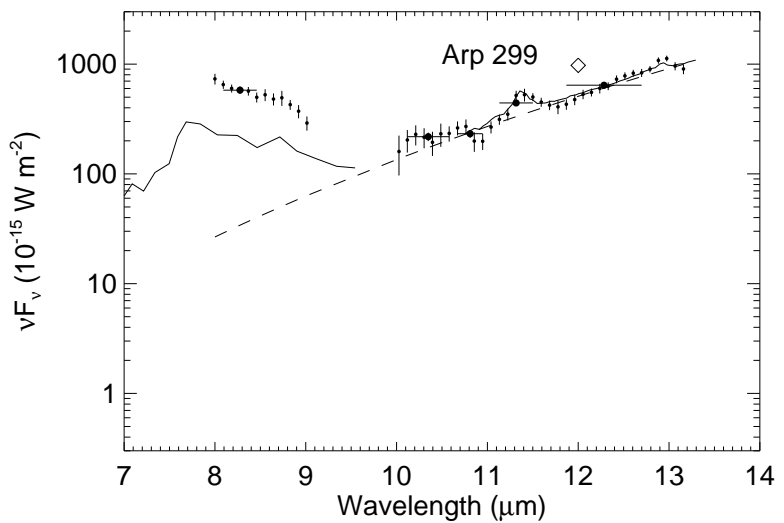
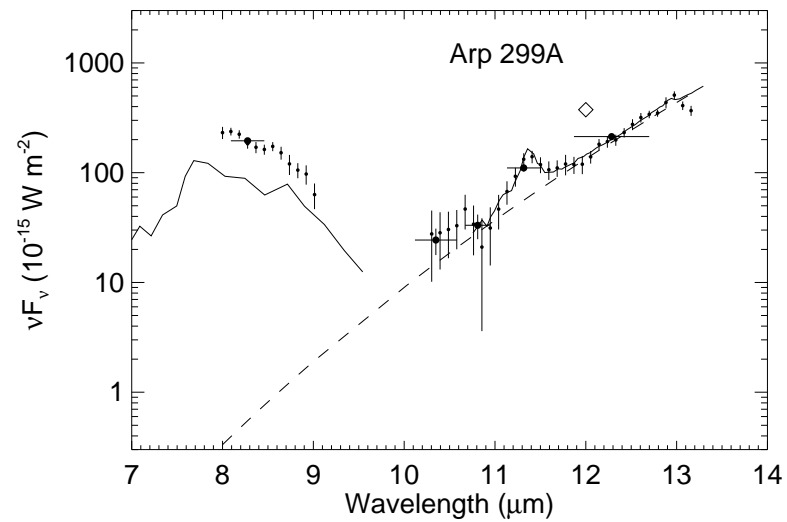
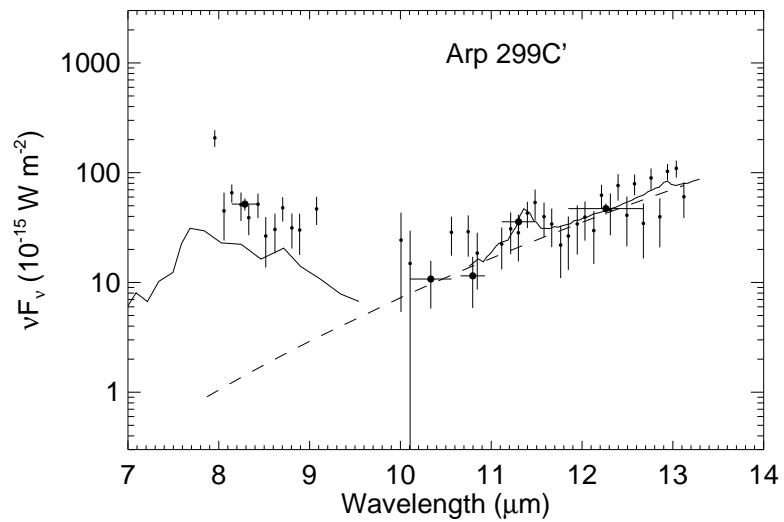
Figure 4. A possible anti-correlation between star formation efficiency and the equivalent width of the 11.3 μm PAH feature is shown.

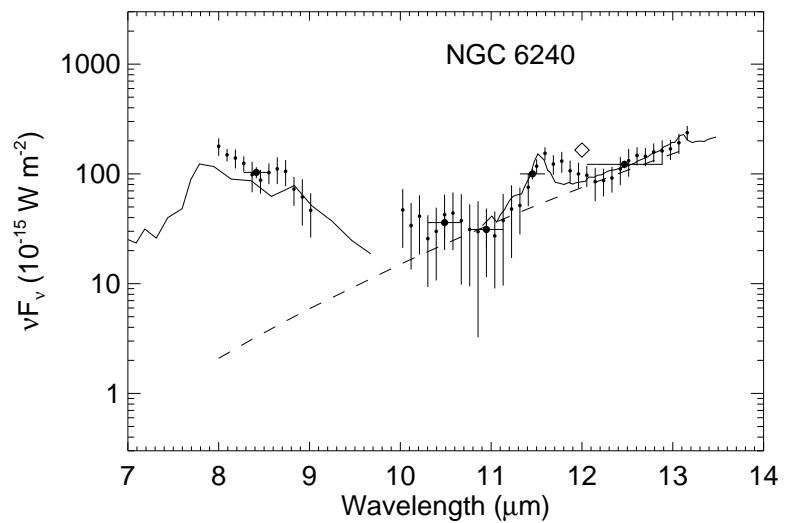
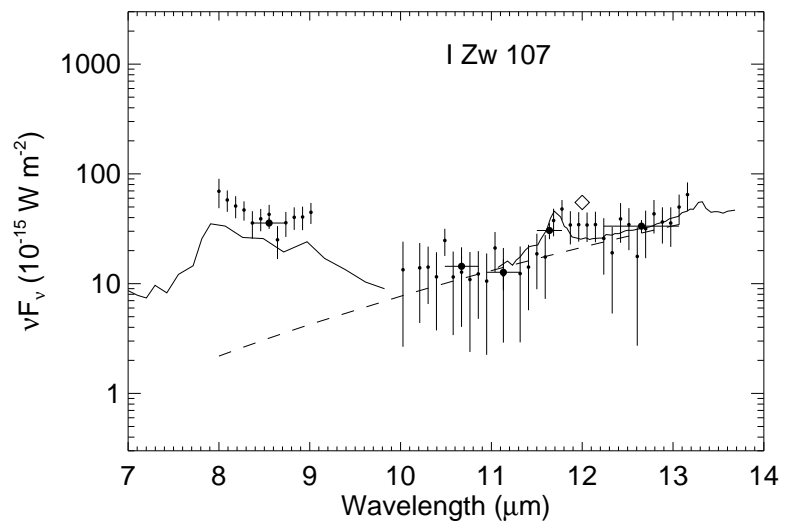
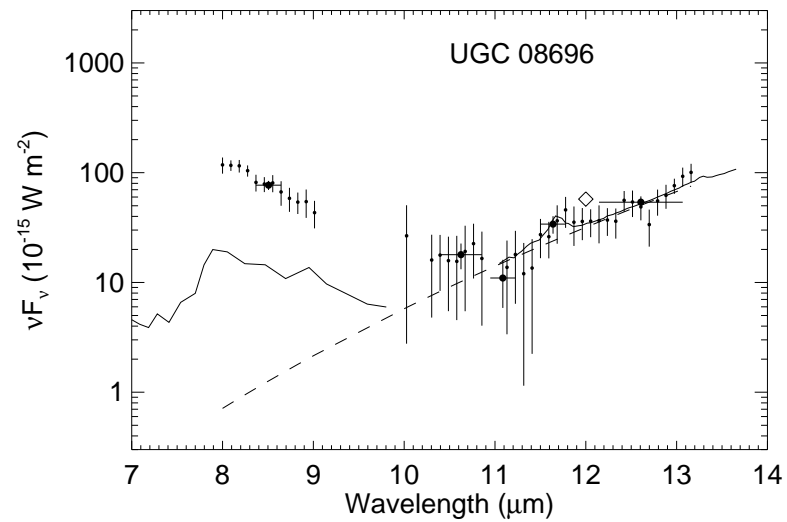
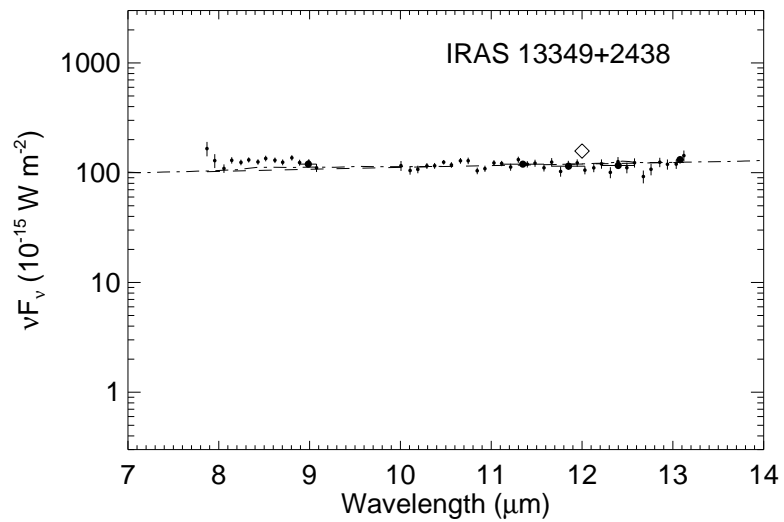


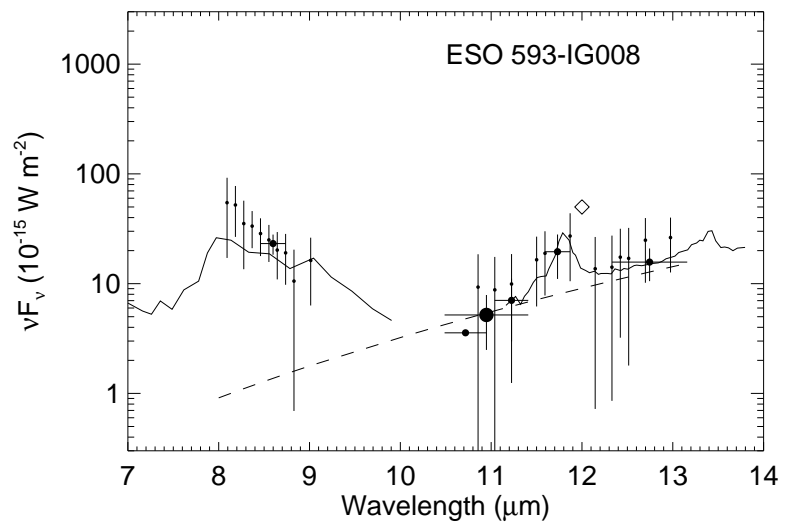
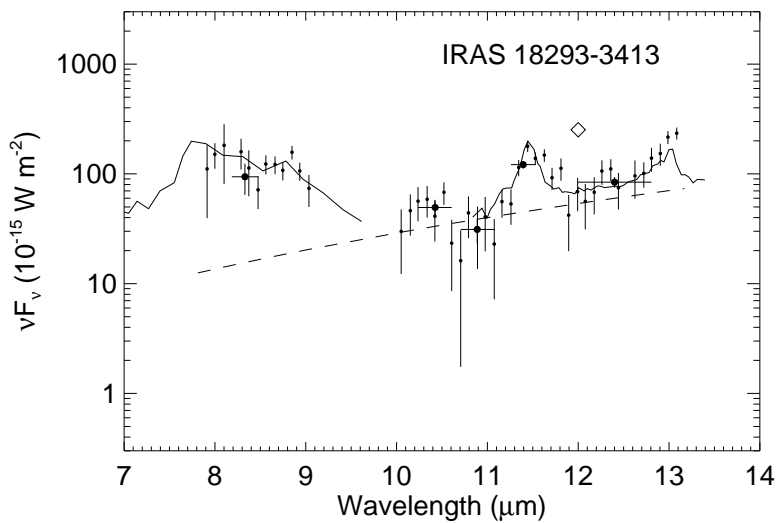
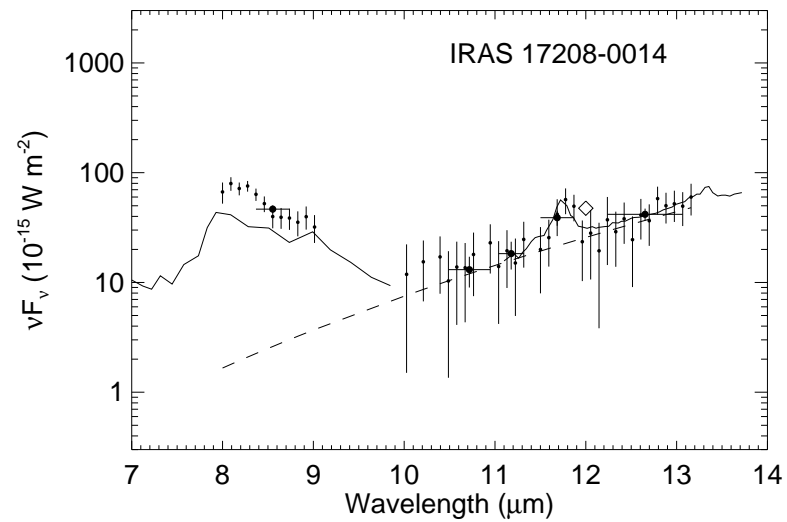
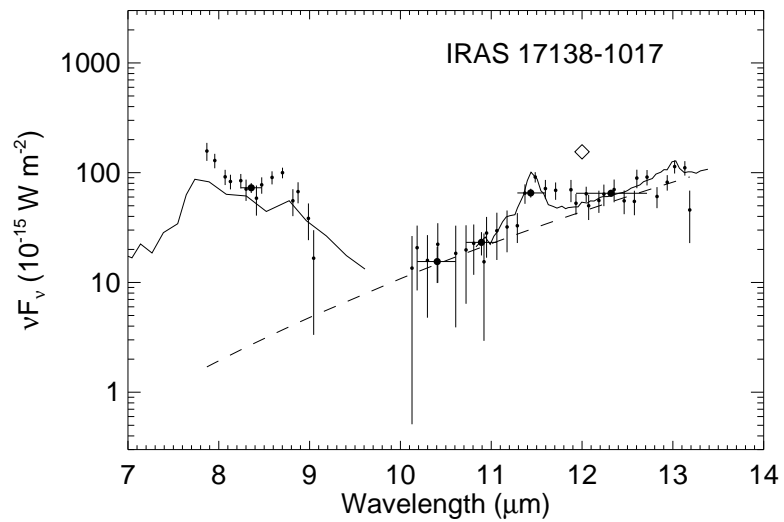


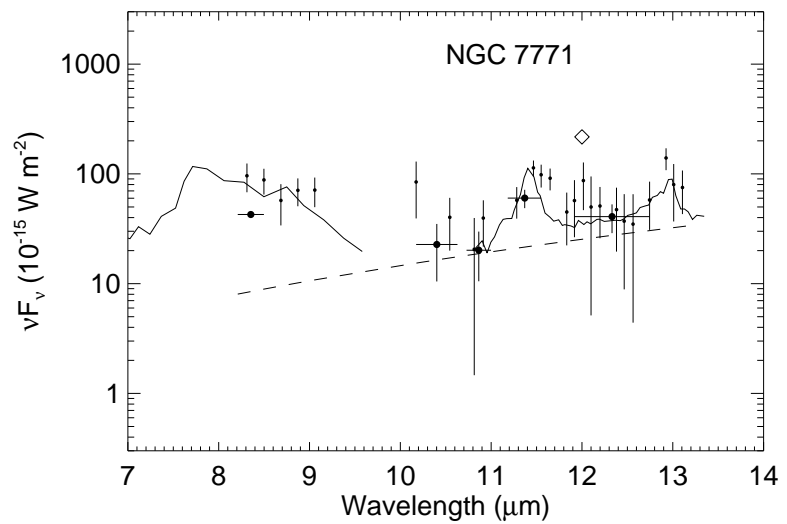
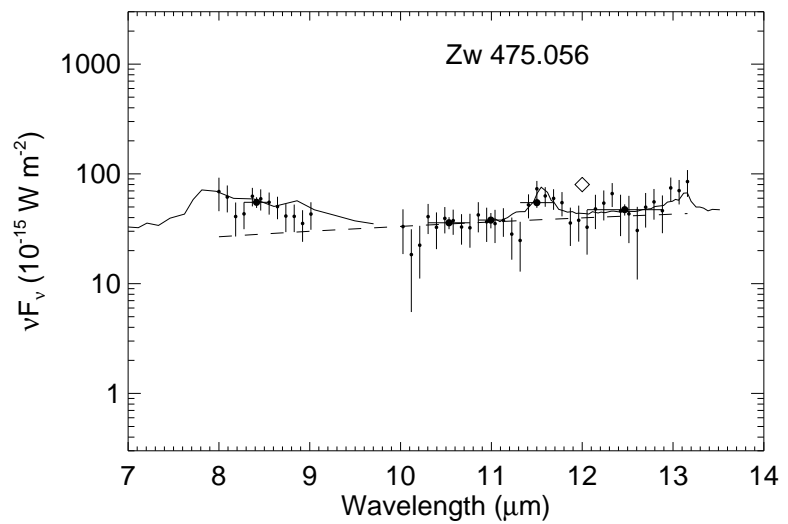
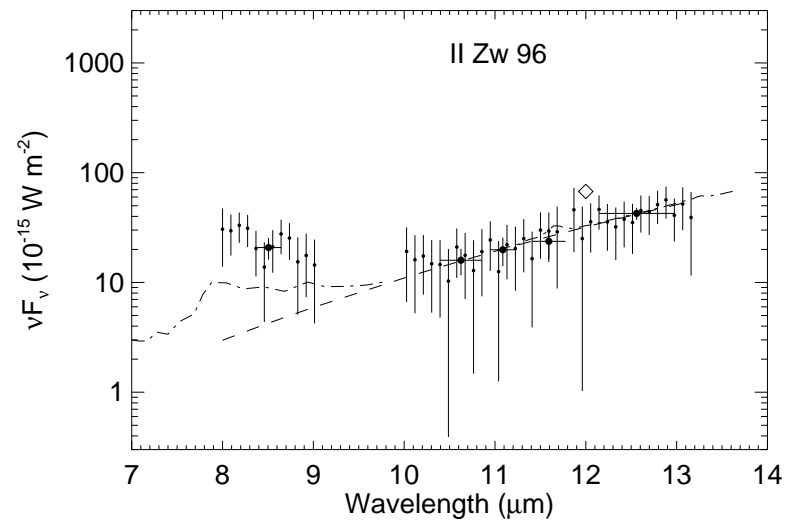
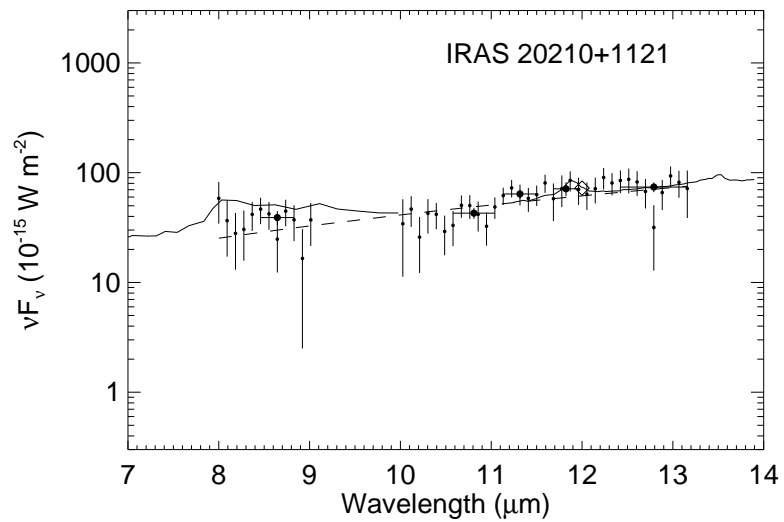


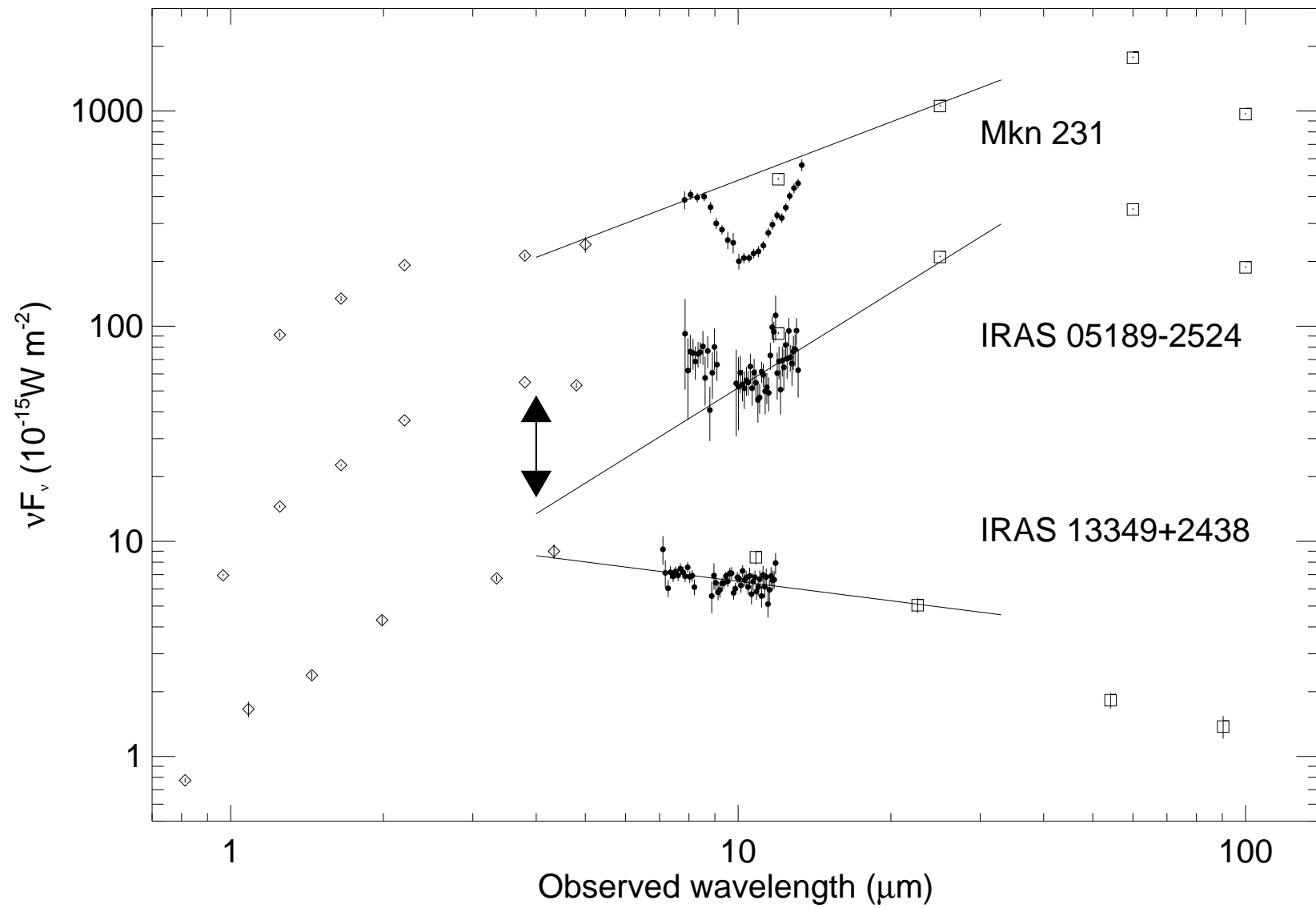




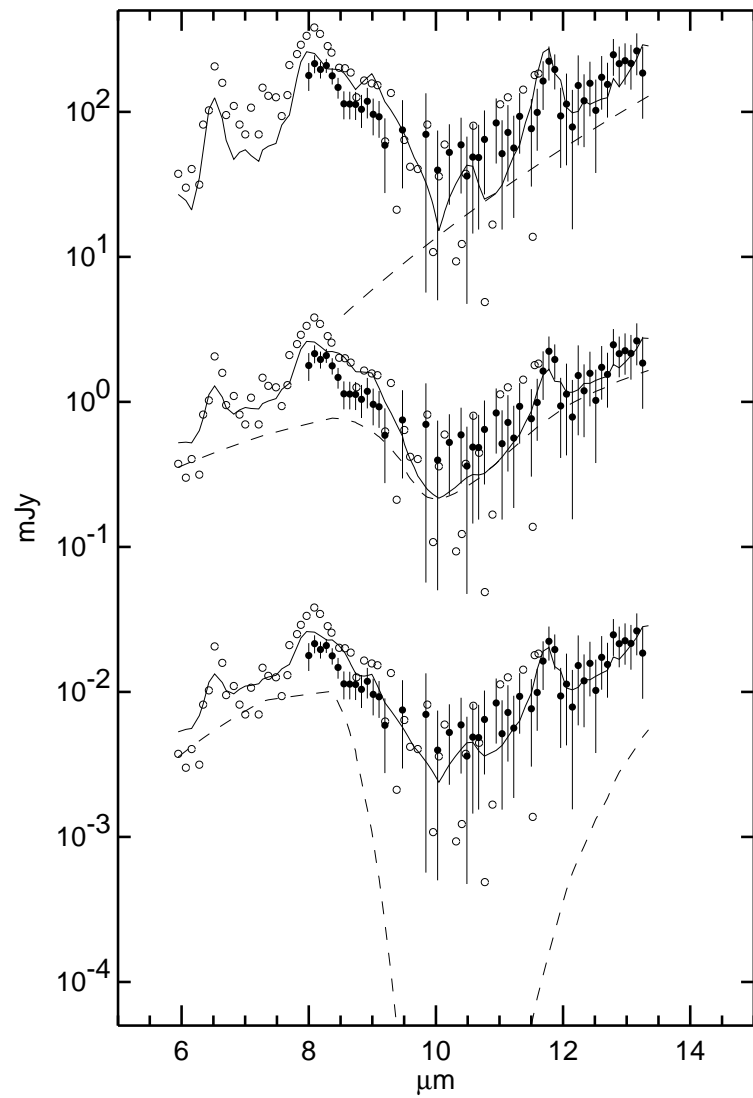




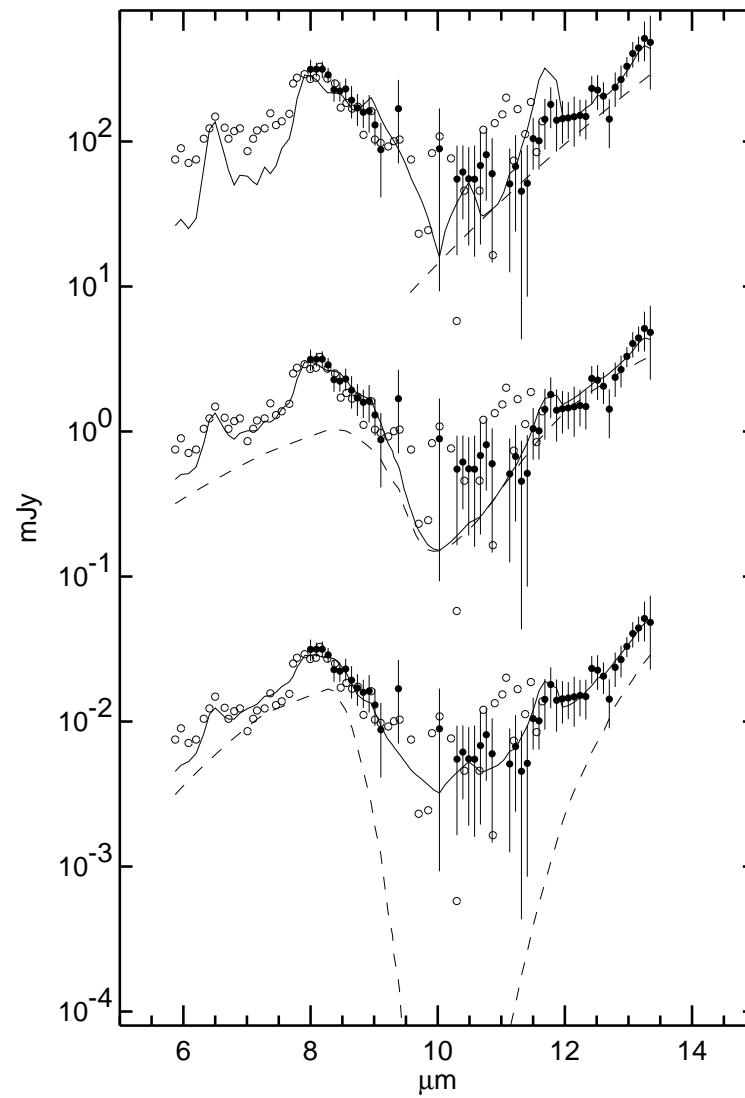




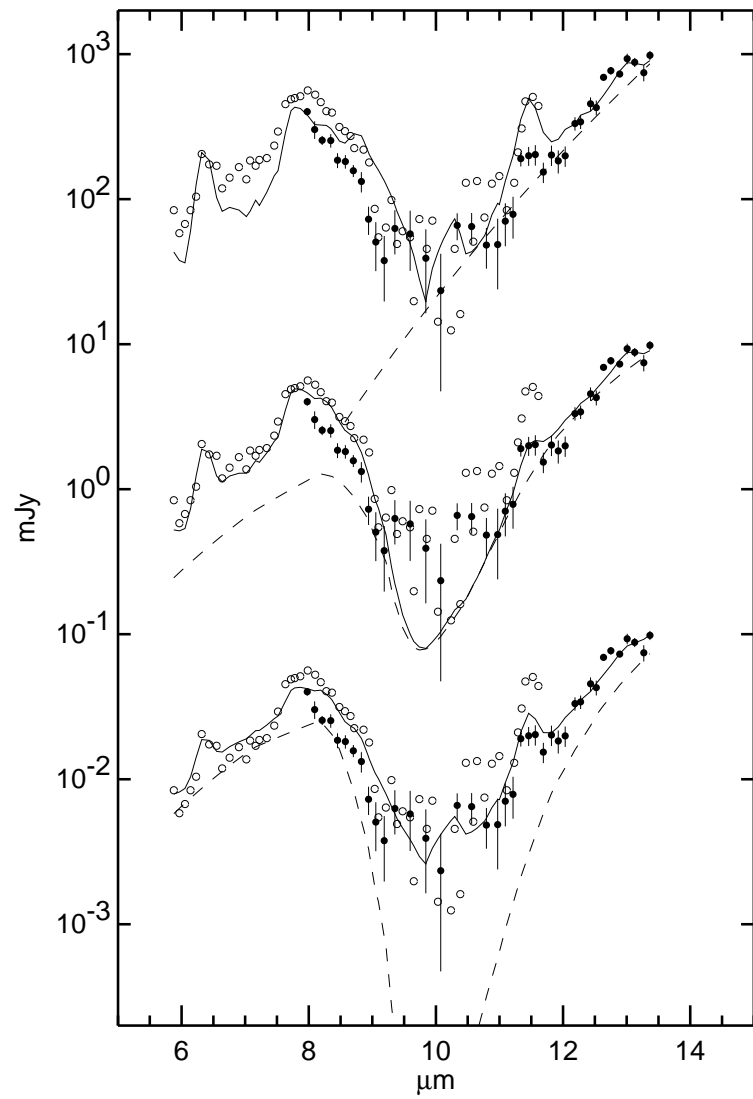
IRAS 17208-0014



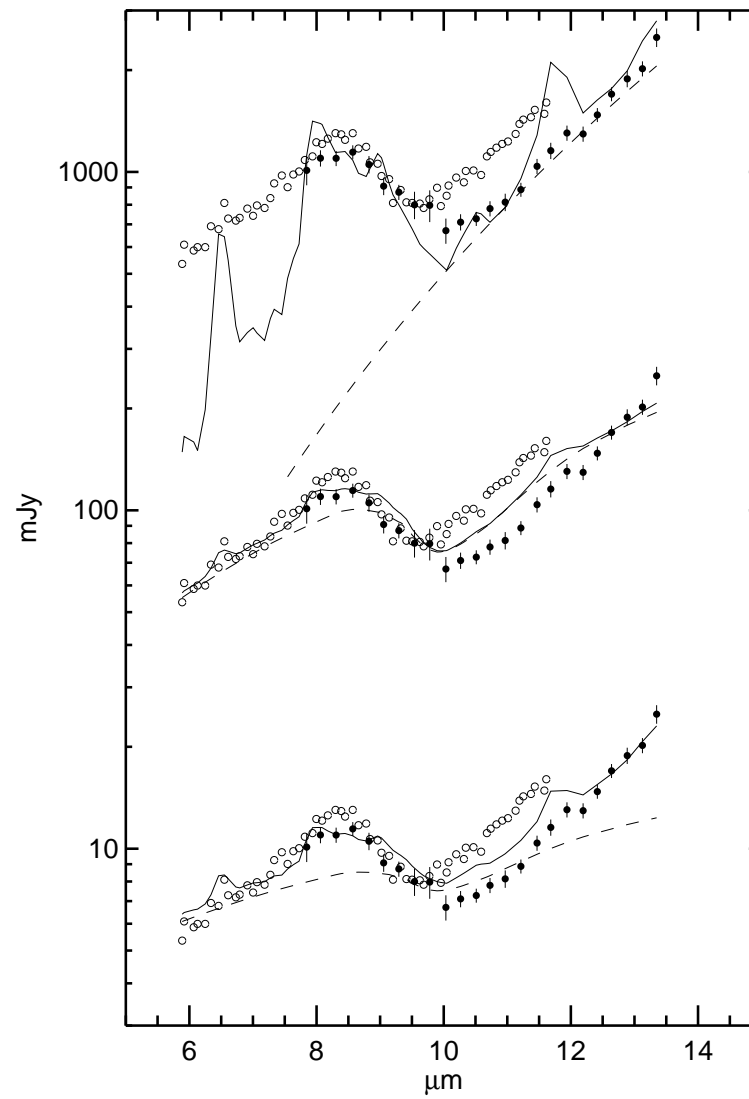
Mkn 273

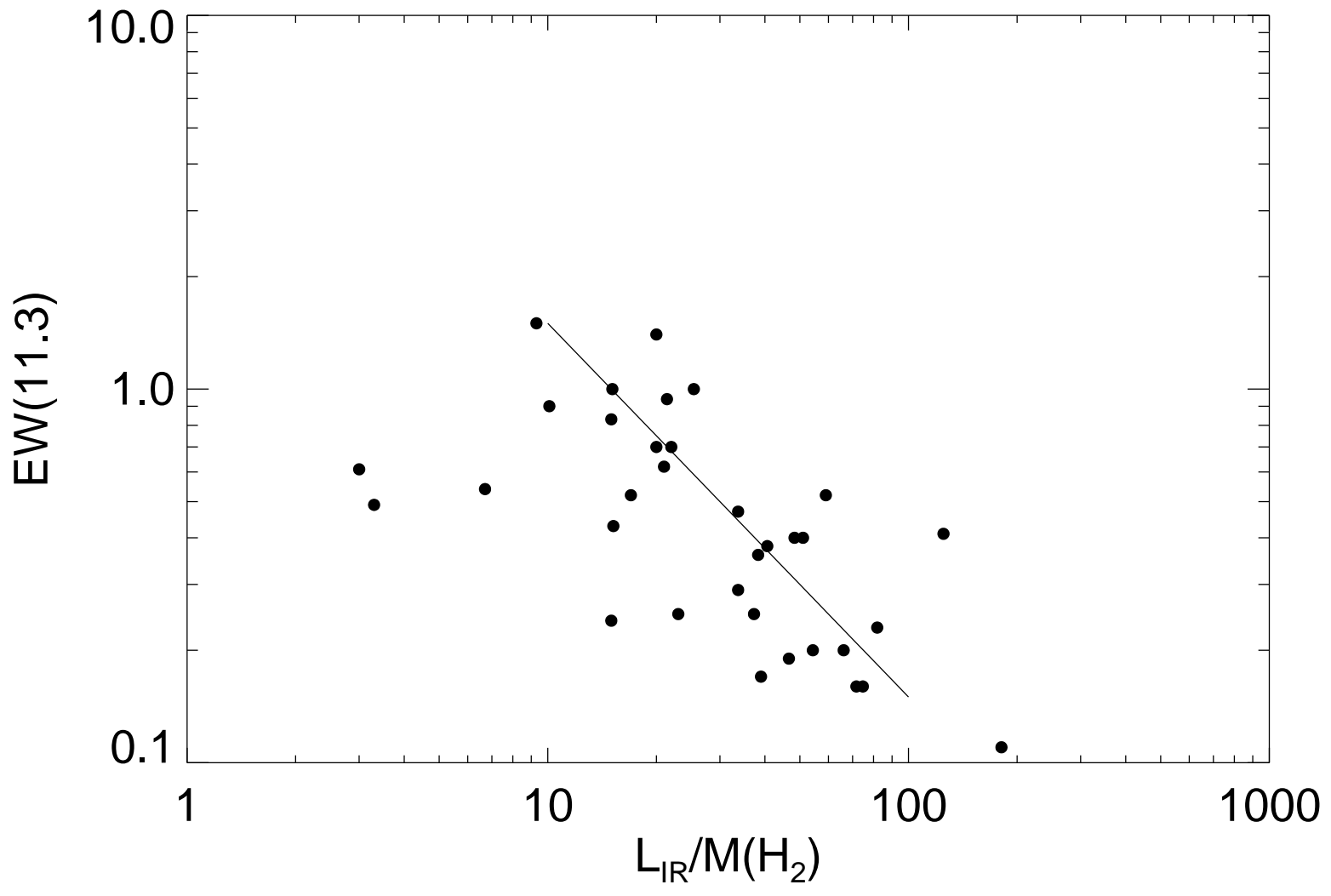


Arp 220



Mkn 231





Tables for 8–13 μm spectroscopy of luminous and ultraluminous infrared galaxies

C. C. Dudley

Institute for Astronomy, 2680 Woodlawn Dr., Honolulu, Hawaii 96822, USA

Table 1. Observing log and adopted redshifts for spectroscopic observations.

Object Name	$\alpha(1950)$ (h m s)	$\delta(1950)$ ($^{\circ}$ ' ")	Ref	z	Ref	Date (UT)	App (")	Chop (")	PA ($^{\circ}$)
Mkn 551	00 26 46.7	+30 16 59	1 ^a	0.0504	2	1995 Aug 14	3.26	20	90
IC 1632	01 05 19.87	-17 46 25.5	1	0.0185	1	1992 Oct 16	5.50	20	90
NGC 695	01 48 27.85	+22 20 06.9	7	0.0327	1	1993 Aug 30	5.50	30	135
NGC 828	02 07 06.80	+38 57 17.5	1	0.0179	1	1992 Oct 14 1992 Oct 15	5.50	20	90
MCG +05-06-036	02 20 23.93	+31 58 13.5	9	0.0380	3	1994 Aug 29	3.88	15	45
IRAS 02528+4350	02 52 54.03	+43 50 51.2	1 ^a	0.1123	2 ^c	1993 Aug 31 1993 Sep 01	2.40 3.26	15	135
IRAS 04154+1755	04 15 28.54	+17 55 21.4	1 ^b	0.0556	2	1995 Mar 19 1995 Mar 20 1995 Mar 21	3.26	20	0
IRAS 05189-2524	05 18 58.88	-25 24 39.4	2 ^c	0.0424	1	1993 Feb 11	3.88	30	90
NGC 2388	07 25 38.1	+33 55 21	8	0.0135	1	1992 Feb 16	5.50	20	90
NGC 2623	08 35 25.27	+25 55 50.2	7	0.0185	1	1992 Feb 17 1993 Feb 12	5.50 3.26	30	90 113
IRAS 09111-1007	09 11 10.78	-10 07 04.1	5	0.0548	2	1995 Mar 19	3.26	20	0
UGC 04881	09 12 38.43	+44 32 29.2	2	0.0399	1	1995 Mar 20	3.26	20	0
IRAS 09433-1531	09 43 19.50	-15 31 10.1	1	0.0527	2	1995 Mar 21	3.26	20?	0
NGC 3110	10 01 32.2	-06 14 02		0.0097	1	1992 Feb 16	5.5	30?	90?
IRAS 10565+2448	10 56 36.17	+24 48 39.9	2 ^c	0.0417	1	1993 Feb 11	3.88	30	90
Arp 299C	11 25 41.19	+58 50 20.9	2 ^c	0.0105	1	1992 Feb 17	5.50	30	...
Arp 299B1	11 25 41.53	+58 50 12.4	6			1991 May 17	5.50	15	45
Arp 299C'	11 25 41.87	+58 50 21.6	2 ^c			1995 Mar 20	3.26	20	0
Arp 299A	11 25 44.19	+58 50 18.3	2			1991 May 18 1995 Mar 19	5.50 3.26	15 20	45 0
UGC 08387	13 18 17.01	+34 24 04.7	7	0.0229	1	1993 Feb 12	3.26	30?	113
IRAS 13349+2438	13 34 57.37	+24 38 18.5	3	0.1076	3	1995 Mar 18	3.26	20	0
UGC 08696	13 42 51.71	+56 08 14.3	2	0.0380	1	1991 May 20 1992 Feb 16	5.50	15 20	90
I Zw 107	15 16 19.29	+42 55 38.2	2	0.0401	1	1995 Mar 18 1995 Mar 19	3.26	20	0
NGC 6240	16 50 27.83	+02 28 57.5	4	0.043	1	1991 May 18	5.50 3.26	15	45
IRAS 17138-1017	17 13 50.7	-10 17 29	5	0.0175	3	1991 May 19	5.50	30	135
IRAS 17208-0014	17 20 47.2	-00 14 15	5	0.0428	3	1993 Aug 30 1993 Aug 31 1993 Sep 01 1994 Aug 29	2.40 3.26 3.88	15	90 45
IRAS 18293-3413	18 29 22.4	-34 13 41.4	1 ^d	0.0182	1	1993 Sep 01	3.26	15	90
ESO 593-IG008	19 11 32.3	-21 24 22	5	0.0487	3	1994 Aug 27 1995 Mar 20	3.88 3.26	20	90 0

Table 1—Continued

Object Name	$\alpha(1950)$ (h m s)	$\delta(1950)$ ($^{\circ}$ ' ")	Ref	z	Ref	Date (UT)	App (")	Chop (")	PA ($^{\circ}$)
						1995 Aug 13		90	
IRAS 20210+1121	20 21 02.58	+11 21 52.5	1	0.0564	2	1994 Aug 28	3.88	15	135
						1995 Aug 13	3.26	20	90
II Zw 96	20 55 05.3	+16 56 03	5	0.0363	3	1994 Aug 29	3.88	15	45
						1995 Aug 14	3.26	20	90
Zw 475.056	23 13 33.13	+25 17 01.6	7	0.0274	1	1993 Aug 31	2.40	15	90
						1993 Sep 01	3.26		

References. — Positions are from (1) this work, (2) CHYT, (3) Hewitt & Burbidge (1989), (4) Eales et al. (1990), (5) Condon et al. (1996), (6) Wynn-Williams et al. (1991), (7) Condon et al. (1990), (8) Condon, Frayer & Broderick (1991), and (9) Clements (1981). Redshifts are from (1) Soifer et al. (1989), (2) Strauss et al. (1992), and (3) Sanders et al. (1995)

^aBrightest optical component

^bBrightest K-band component

^cFrom figure rather than table

^d8–13 μm peak up position

^eThe redshift for this source has been dropped from later versions of this catalog. Crawford et al. (1996) failed to detect this source at radio wavelengths, and propose that it may be attributable to Galactic infrared cirrus. The present spectrum (see Fig. 1) is not typical of cirrus, so the source has been retained here. The reported sensitivities of Crawford et al. (1996) suggest that this source is under-luminous at 20 cm by a factor of at least 8 compared to the usual far infrared–radio correlation (Helou, Soifer, & Rowan-Robinson 1985).

Table 2. Calibration stars

Object Name	Alternate Name(s)	Date (UT)	HR (#)	$F_{\nu}(10.1)$ (Jy)	Ref	T (K)
Mkn 551	IV Zw 023	1995 Aug 14	7001	39.8	1	11000
IC 1632	Arp 236, ESO 541-IG 023	1992 Oct 16	8775	413	1	3000
NGC 695	UGC 01315, V Zw 123	1993 Aug 30	7001	39.8	1	11000
NGC 828	UGC 01655, VI Zw 177	1992 Oct 14	2491	147	1	10000
		1992 Oct 15	8775	413	1	3000
MCG +05-06-036	V Zw 233, Mkn 1034	1994 Aug 29	0188	57.5	3	5800
IRAS 02528+4350		1993 Aug 31	7001	39.8	1	11000
		1993 Sep 01				
IRAS 04154+1755		1995 Mar 19	1708	238	1	5500
		1995 Mar 20	1457	648	1	5000
		1995 Mar 21	1457	648	1	5000
IRAS 05189-2524		1993 Feb 11	2943	80.1	1	8000
NGC 2388	UGC 03870	1992 Feb 16	3748	150	1	4000
NGC 2623	UGC 04509, ARP 243, VV 079	1992 Feb 17	4518	18.1	2	6000
		1993 Feb 12	2943	80.1	1	8000
IRAS 09111-1007		1995 Mar 19	1708	238	1	5500
UGC 04881	Arp 55, VV 155	1995 Mar 20	1457	648	1	5000
IRAS 09433-1531		1995 Mar 21	1457	648	1	5000
NGC 3110	MCG -01.26-014	1992 Feb 16	3748	150	1	4000
IRAS 10565+2448		1993 Feb 11	3873	15.4	2	5000
Arp 299C ^a		1992 Feb 17	4518	18.1	2	6000
Arp 299B1	NGC 3690	1991 May 17	5340	738	1	4400
Arp 299C ^f		1995 Mar 20	4518	18.1	2	6000
Arp 299A	IC 0694	1991 May 18	4534	7.31	1	8700
		1995 Mar 19	4518	18.1	2	6000
UGC 08387	IC 883, Arp 193, I Zw 56, VV 821	1993 Feb 12	5235	11.5	2	6000
IRAS 13349+2438		1995 Mar 18	5235	11.5	2	6000
UGC 08696	Mkn 273, VV 851, I Zw 071	1991 May 20	4535	7.31	1	8700
	MCG +09.23-004	1992 Feb 16	3748	150	1	4000
I Zw 107	Mkn 848	1995 Mar 18	5235	11.5	2	6000
		1995 Mar 19	5240	738	1	4400
NGC 6240	UGC 10592, VV 617	1991 May 18	4534	7.31	1	8700
			7001	39.8	1	11000
IRAS 17138-1017		1991 May 19	5340	738	1	4400
IRAS 17208-0014		1993 Aug 30	7001	39.8	1	11000
		1993 Aug 31				
		1993 Sep 01				
		1994 Aug 29				
IRAS 18293-3413		1993 Sep 01	7001	39.8	1	11000
ESO 593-IG008		1994 Aug 27	7264	8.32	3	9000
		1995 Mar 20	1457	648	1	5000
		1995 Aug 13	7557	33.3	2	9000
IRAS 20210+1121		1994 Aug 28	7949	39.8	3	6000
		1995 Aug 13	7557	33.3	2	9000
II Zw 96		1994 Aug 29	7949	39.8	3	6000
		1995 Aug 14	7001	39.8	1	11000
Zw 475.056	IC 5298, MCG +04.54-038	1993 Aug 31	7001	39.8	1	11000
		1993 Sep 01				

^aThis spectrum was previously reported in Dudley & Wynn-Williams (1993); it has now been recalibrated to be ~10% fainter.

Table 3. Spectral measurements of galaxies.

Object Name	α	I(11.3) (10^{-15} W m $^{-2}$)	EW(11.3) (μ m)	$\frac{f_{\nu \text{ source}(8.2)}}{f_{\nu \text{ model}(8.2)}}$	I([SiIV]) (10^{-15} W m $^{-2}$)	I([NeII]) (10^{-15} W m $^{-2}$)
Mkn 551	11.6 \pm 0.6	<2 0.85 \pm 0.06 1.6 \pm 0.3	...	0.8 \pm 1.9	1.4 \pm 0.2	<0.9 ...
IC 1632	8.3 \pm 0.2	1.56 \pm 0.04 0.8 \pm 0.2	0.43 \pm 0.25	2.2 \pm 0.2	<0.9	<1
NGC 695	9.8 \pm 0.9	0.54 \pm 0.03 <2	1.4 \pm 4.5	0.8 \pm 0.2	<0.3	...
NGC 828	2.4 \pm 0.8	0.84 \pm 0.05 <1	1 \pm 2	1.2 \pm 0.3	<1	<2
MCG +05-06-036	1.4 \pm 0.6	0.77 \pm 0.05 <1	0.9 \pm 2.0	0.8 \pm 0.2	<0.9	...
IRAS 02528+4350	0.6 \pm 0.3	<0.4 <0.9	-0.012 \pm 0.023	<0.9	<5	...
IRAS 04154+1755	5.8 \pm 0.3	0.55 \pm 0.04 <2	0.34 \pm 0.33	1.1 \pm 0.2	<0.5	...
IRAS 05189-2524	2.47 \pm 0.05	2.05 \pm 0.05 2.5 \pm 0.3	0.20 \pm 0.04 0.6 \pm 0.1	1.02 \pm 0.09	<1	...
NGC 2388	6.0 \pm 0.1	3.11 \pm 0.04 <0.9	0.94 \pm 0.49	0.85 \pm 0.07	<0.7	1.2 \pm 0.3
NGC 2623	10.6 \pm 0.4	0.76 \pm 0.04 <0.6	0.52 \pm 0.70	2.1 \pm 0.3	<0.6	0.8 \pm 0.3
IRAS 09111-1007	8.0 \pm 0.4	0.16 \pm 0.03 <0.7	0.17 \pm 0.27	1.6 \pm 0.5	<0.4	...
IRAS 09433-1531	7.8 \pm 0.5	0.54 \pm 0.03 1.5 \pm 0.3	0.59 \pm 0.98	1.2 \pm 0.2	<0.4	...
NGC 3110	5.1 \pm 0.5	1.46 \pm 0.04 <0.7	1.5 \pm 2.5	0.8 \pm 0.1	<0.7	<0.8
IRAS 10565+2448	11.1 \pm 0.3	0.73 \pm 0.04 2.0 \pm 0.2	0.40 \pm 0.41 0.27 \pm 0.04	2.4 \pm 0.2	<0.7	...
Arp 299C	4.20 \pm 0.06	1.99 \pm 0.04 <2	0.28 \pm 0.06	1.07 \pm 0.06	<0.6	2.0 \pm 0.2
Arp 299B1	6.64 \pm 0.05	1.21 \pm 0.06 <0.9	0.079 \pm 0.014	3.3 \pm 0.2	<0.5 ^a	0.7 \pm 0.2 ^a
Arp 299C'	9.67 \pm 0.01	0.54 \pm 0.04 4 \pm 1	0.27 \pm 0.02 0.13 \pm 0.04	2.7 \pm 0.3	<0.7	<0.9
Arp 299	8.21 \pm 0.03	5.10 \pm 0.08 1.4 \pm 0.5	0.16 \pm 0.02	2.8 \pm 0.1	<2	<4
Arp 299A	15.8 \pm 0.1	2.29 \pm 0.05 0.9 \pm 0.2	0.41 \pm 0.19	2.6 \pm 0.1	<0.8	<2
UGC 08387	11.1 \pm 0.4	0.65 \pm 0.03 <0.8	0.62 \pm 0.93	2.4 \pm 0.2	<0.4	0.9 \pm 0.2
IRAS 13349+2438	1.38 \pm 0.08	<0.1 <0.8	-0.020 \pm 0.008	1.05 \pm 0.04	<0.5	...
UGC 08696	10.4 \pm 0.2	0.35 \pm 0.04 <0.7	0.16 \pm 0.14	6.0 \pm 0.6	<0.7	...
I Zw 107	6.7 \pm 0.3	0.60 \pm 0.04 2.9 \pm 0.6	0.38 \pm 0.36	1.6 \pm 0.2	<0.5	...
NGC 6240	9.8 \pm 0.2	2.20 \pm 0.05 1.2 \pm 0.3	0.47 \pm 0.26	1.4 \pm 0.2	<1	<2
IRAS 17138-1017	8.7 \pm 0.2	1.54 \pm 0.04 <1	0.56 \pm 0.40	1.4 \pm 0.1	<0.8	<0.8
IRAS 17208-0014	7.8 \pm 0.2	0.77 \pm 0.04 3.7 \pm 0.5	0.40 \pm 0.35 0.8 \pm 0.3	1.7 \pm 0.1	<0.6	...
IRAS 18293-3413	4.4 \pm 0.1	3.35 \pm 0.05 <1	0.83 \pm 0.43	0.7 \pm 0.2	<1	<1
ESO 593-IG008	6.7 \pm 0.6	0.47 \pm 0.05 <1	0.7 \pm 1.4	1.4 \pm 0.3	<0.6	...
IRAS 20210+1121	3.2 \pm 0.1	0.58 \pm 0.05 <1	0.11 \pm 0.04	0.8 \pm 0.1	<0.7	...
II Zw 96	6.9 \pm 0.2	<0.1 <0.9	-0.015 \pm 0.022	2.4 \pm 0.5	<0.7	...
Zw 475.056	2.0 \pm 0.1	0.82 \pm 0.04 <2	0.25 \pm 0.13	1.0 \pm 0.1	<0.7	<1
NGC 7771	4.0 \pm 0.3	1.97 \pm 0.06	1 \pm 1	<2	<1	<2

^aMeasured from high-resolution spectrum.

Table 4. Spectral classification and other observables.

Object Name	8–13 μ m Class	Optical Class	Ref	Infrared Photometry (Jy)				Ref	$\log \frac{L_{\text{IR}}}{L_{\odot}}$	$\frac{L_{\text{IR}}}{M(H_2)}$ $\left(\frac{L_{\odot}}{M_{\odot}}\right)$	Ref
				12 μ m	25 μ m	60 μ m	100 μ m				
Mkn 551	PAH	H II	3	0.2415	0.7986	4.659	5.686	2	11.72	...	
IC 1632	PAH	H II	1	0.98	3.43	22.19	30.32	1	11.54	15.2	1
NGC 695	PAH	H II	1	0.49	0.81	7.61	13.80	1	11.64	20.0	1
NGC 828	PAH	L	6	0.78	1.04	12.03	24.38	1	11.34	15.1	1
MCG +05–06–036	PAH	Sy1	2	0.2451	.6944	6.475	11.45	2	11.71	10.1	5
IRAS 02528+4350	Flat	...		0.5046	2.293	2.762	...	2	12.54	...	
IRAS 04154+1755	PAH	Sy2	7	0.2030	0.7141	3.822	5.84	2	11.75	...	
IRAS 05189–2524	PAH	Sy2	1	0.74	3.50	13.95	12.52	1	12.09	54.3	1
NGC 2388	PAH	H II	1	0.49	1.96	16.36	29.68	1	11.21	21.4	4
NGC 2623	PAH	L or Sy2	1	0.24	1.85	25.72	27.36	1	11.55	59.0	1
IRAS 09111–1007	PAH	...		0.17 ^a	0.57	7.19	11.04	1	11.99	39	1
UGC 04881	PAH?	H II	1	0.16	0.62	6.53	10.21	1	11.70	17.6	1
IRAS 09433–1531	PAH	...		0.1876	0.7174	4.463	4.698	2	11.72	...	
NGC 3110	PAH	H II	1	0.58	1.10	11.68	23.16	1	11.22	9.3	1
IRAS 10565+2448	PAH	H II	1	0.21	1.21	12.53	16.06	1	11.99	48.3	1
Arp 299C	PAH	...		0.39	2.2	3			
Arp 299B1	PAH+Sil	H II	3	1.7	6.9	3			
Arp 299C'	PAH			0.23	4			
Arp 299	PAH+Sil			3.90	24.14	121.64	122.45	1	11.90	71.7	1
Arp 299A	PAH+Sil	H II	3	1.11	12.4	53	64	3,5	11.7	125	7

Table 4—Continued

Object Name	8–13 μ m Class	Optical Class	Ref	Infrared Photometry (Jy)				Ref	$\log \frac{L_{\text{IR}}}{L_{\odot}}$	$\frac{L_{\text{IR}}}{M(\text{H}_2)}$ ($\frac{L_{\odot}}{M_{\odot}}$)	Ref
				12 μ m	25 μ m	60 μ m	100 μ m				
UGC 08387	PAH	L	1	0.26	1.37	13.69	24.90	1	11.58	21	3
IRAS 13349+2438	Flat	Sy1	4	0.6308	0.8406	0.6114	...	2	12.21	...	
UGC 08696	Sil	L	1	0.23	2.30	22.09	22.44	1	12.14	74.7	1
I Zw 107	PAH	H II L?	1	0.22	1.40	9.15	10.04	1	11.85	40.6	1
NGC 6240	PAH	L	1	0.66	3.67	22.80	27.35	1	11.83	33.7	1
IRAS 17138–1017	PAH	H II	1	0.62	2.09	15.84	20.88	1	11.39	...	
IRAS 17208–0014	PAH	H II	1	0.17 ^a	1.71	34.67	37.65	1	12.40	51	2
IRAS 18293–3413	PAH	H II	1	1.01	4.03	35.92	50.71	1	11.74	15	2
ESO 593–IG008	PAH	L	1	0.20	0.47	6.59	10.26	1	11.86	22	2
IRAS 20210+1121	Flat	Sy2	5	0.2948	1.398	3.385	2.682	2	11.87	181	6
II Zw 96	PAH?	H II	1	0.27	2.28	13.24	11.61	1	11.89	...	
Zw 475.056	PAH	Sy2	1	0.32	1.88	8.75	11.64	1	11.53	37.3	1
NGC 7771	PAH	H II	1	0.87	2.18	20.46	37.42	1	11.35	25.4	1

^aFrom *IRAS* Faint Source Catalog (Moshir et al. 1990).

References. — Optical spectral classifications are from (1) Veilleux et al. (1995), and (2) Mazzarella & Balzano (1986), (3) Mazzarella & Boroson (1993), (4) Beichman et al. (1986), (5) Perez et al. (1990), (6) Keel & Windhorst (1991), and (7) Crawford et al. (1996). Infrared fluxes are from (1) Soifer et al. (1989), (2) Moshir et al. (1990), (3) Wynn-Williams et al. (1991), (4) Keto et al. (1997), and (5) Joy et al. (1989). L_{IR} to $M(\text{H}_2)$ ratios are from (1) Sanders, Scoville & Soifer (1991), (2) Mirabel et al. (1990), (3) Solomon et al. (1997), (4) Solomon & Sage (1988), (5) Krügel, Chini & Steppe (1990), (6) Horellou et al. (1995), and (7) Sargent & Scoville (1991).

Table 5. 60 μm Flux limited subsample.

Object Name	8–13 μm Class	Ref	$\log \frac{L_{\text{IR}}}{L_{\odot}}$	$\log \frac{F_{\nu}(12)}{F_{\nu}(60)}$
UCG 8058 (Mkn 231)	sil	2	12.53	-1.26
IRAS 17208–0014	PAH	1	12.40	-2.1
UCG 9913 (Arp 220)	sil	2	12.18	-2.2
UCG 8696 (Mkn 273)	sil	1	12.14	-2.0
IRAS 05189–2524	PAH	1	12.09	-1.3
IRAS 10565+2448	PAH	1	11.99	-1.8
Arp 299	PAH + sil	1	11.90	-1.49
II Zw 96	PAH?	1	11.89	-1.7
NGC 6240	PAH	2,1	11.83	-1.5
IRAS 18293–3413	PAH	1	11.74	-1.55
NGC 7469	PAH	2	11.60	-1.24
UCG 8387	PAH	1	11.58	-1.7
NGC 1614	PAH	2	11.58	-1.36
NGC 2623	PAH	1	11.55	-2.0
IC 1623	PAH	1	11.54	-1.4
III Zw 35	unknown		11.54	< -2.0
NGC 34	unknown		11.41	-1.6
Mkn 331	PAH	2	11.41	-1.5
ESO 507-G070	unknown		11.41	-1.7
IRAS 17138–1017	PAH	1	11.39	-1.4
NGC 7771	PAH	1	11.35	-1.4
NGC 828	PAH	1	11.34	-1.2
NGC 1068	sil	2	11.27	-0.702
NGC 3110	PAH	1	11.22	-1.3
NGC 2388	PAH	1	11.21	-1.5

References. — Classifications are from (1) this work or (2) RASW

Table 6. Previously published results.

Object	EW(11.3)	$\frac{L_{\text{IR}}}{M(\text{H}_2)}$	
Name	(μm)	($\frac{L_{\odot}}{M_{\odot}}$)	Ref
NGC 7469	0.19	46.6	1
NGC 1614	0.36	38.3	1
NGC 7714	0.25	23.0	1
NGC 0660	0.52	17.	2
NGC 6946	0.49	3.3	2
IC 342	0.61	3.0	2
NGC 0253	0.24	15	2
NGC 6240	0.29	33.7	1
IC 4553 (Arp 220)	0.23	81.9	1
Mkn 331	0.70	20.0	1
NGC 4194	0.20	66.1	1
NGC 2782	0.54	6.7	1

References. — L_{IR} to $M(\text{H}_2)$ ratios are from (1) Sanders et al. (1991) or (2) Mirabel et al. (1990).